8–13 μm SPECTROSCOPY OF YOUNG STELLAR OBJECTS: EVOLUTION OF THE SILICATE FEATURE

Jacqueline E. Kessler-Silacci,[1,2] Lynne A. Hillenbrand,[3] Geoffrey A. Blake,[2,4] and Michael R. Meyer[5]

ABSTRACT

Silicate features arising from material around pre–main-sequence stars are useful probes of the star and planet formation process. In order to investigate possible connections between dust processing and disk properties, 8–13 μm spectra of 34 young stars, exhibiting a range of circumstellar environments and including spectral types A–M, were obtained using the Long Wavelength Spectrometer at the W. M. Keck Observatory. The broad 9.7 μm amorphous silicate (Si—O stretching) feature that dominates this wavelength regime evolves from absorption in young, embedded sources, to emission in optically revealed stars, and to complete absence in older "debris" disk systems for both low- and intermediate-mass stars. This is similar to the evolutionary pattern seen in *Infrared Space Observatory* (*ISO*) observations of high/intermediate-mass young stellar objects (YSOs). The peak wavelength and FWHM are centered about 9.7 and ∼2.3 μm, respectively, corresponding to amorphous olivine, with a larger spread in FWHM for embedded sources and in peak wavelength for disks. In a few of our objects that have been previously identified as class I low-mass YSOs, the observed silicate feature is more complex, with absorption near 9.5 μm and emission peaking around 10 μm. Although most of the emission spectra show broad classical features attributed to amorphous silicates, small variations in the shape/strength may be linked to dust processing, including grain growth and/or silicate crystallization. For some of the Herbig Ae stars in the sample, the broad emission feature has an additional bump near 11.3 μm, similar to the emission from crystalline forsterite seen in comets and the debris disk β Pictoris. Only one of the low-mass stars, Hen 3-600A, and one Herbig Ae star, HD 179218, clearly show strong, narrow emission near 11.3 μm. We study quantitatively the evidence for evolutionary trends in the 8–13 μm spectra through a variety of spectral shape diagnostics. Based on the lack of correlation between these diagnostics and broadband infrared luminosity characteristics for silicate emission sources, we conclude that although spectral signatures of dust processing are present, they cannot be connected clearly to disk evolutionary stage (for optically thick disks) or optical depth (for optically thin disks). The diagnostics of silicate absorption features (other than the central wavelength of the feature), however, are tightly correlated with optical depth and thus do not probe silicate grain properties.

Subject headings: circumstellar matter — infrared: stars — planetary systems: protoplanetary disks — stars: formation — stars: pre–main-sequence

1. INTRODUCTION: SILICATES AND STAR FORMATION

Circumstellar disks are found around most, if not all, young stars. At least 5% of these circumstellar disks are likely planet forming (Marcy et al. 2000), and it is commonly believed that our solar system formed from a solar nebula similar to circumstellar disks found around young stars. Initially these disks are composed of gas and dust from the interstellar medium (ISM). Theoretical models predict that collisions between grains and subsequent coagulation result in modified grain size distributions and eventually the growth of planetesimals (Weidenschilling & Cuzzi 1993). However, observational evidence of this process remains elusive (Beckwith et al. 2000). One way to gain insight into the process of grain growth, planetesimal evolution, and eventually planet formation is to constrain the effects of these processes on the observed mid-infrared spectra from circumstellar dust. Grain growth and changes in composition due to dust processing in circumstellar disks can have dramatic effects on the observed spectrum of the dust in emission and absorption. In this contribution, we attempt to quantify those effects and place them in the context of modern theories of disk evolution and planet formation.

Dust in the ISM, and thus in the early stages of star formation, consists primarily of oxygen-rich silicates and carbon-rich grains (for summary see Pollack et al. 1994) from a wide range of sources, including stellar atmospheres, novae, and supernovae. These silicates are either olivines ($Mg_{2x}Fe_{2(1-x)}SiO_4$), ranging from fayalite ($x = 0$) to forsterite ($x = 1$), or pyroxenes ($Mg_xFe_{(1-x)}SiO_3$), ranging from ferrosillite ($x = 0$) to enstatite ($x = 1$). Silicate condensates formed in supernovae and during star formation are primarily Fe-rich and amorphous, but at high temperatures, Mg-rich crystalline silicates (i.e., pure forsterite and enstatite) are produced. The fraction of pyroxenes versus olivines depends on both temperature and pressure. For a given pressure, the pyroxenes (e.g., enstatite) dominate at low temperatures and becomes less abundant with increasing temperature (at equilibrium). The olivines (e.g., forsterite) form a significant fraction of the mixture only for a narrow region in pressure-temperature space.

The low temperatures of the ISM are expected to result in amorphous mixtures of olivines and pyroxenes, with olivine the dominant component. Indeed, strong smooth features near 9.7 (Si—O stretching mode) and 18.5 μm (O—Si—O bending mode) are observed in absorption along lines of sight through the diffuse ISM (Whittet et al. 1997; Bouwman et al. 2001).

[1] Department of Astronomy, University of Texas, C-1400, Austin, TX 78712.
[2] Division of Chemistry and Chemical Engineering, California Institute of Technology, MS 105-24, Pasadena, CA 91125.
[3] Division of Physics, Mathematics, and Astronomy, California Institute of Technology, 770 South Wilson Avenue, MS 103-33, Pasadena, CA 91125.
[4] Division of Geological and Planetary Sciences, California Institute of Technology, 1200 East California Boulevard, MS 170-25, Pasadena, CA 91125.
[5] Steward Observatory, University of Arizona, 933 North Cherry Avenue, Tucson, AZ 85721.

Molecular clouds also possess a mixture of olivines and pyroxenes, which are expected to remain amorphous owing to cosmic-ray impacts; a broad structureless band centered near 10 μm is observed toward several objects (Willner et al. 1982; Pegourie & Papoular 1985; Whittet et al. 1988; Bowey et al. 1998). Observations by Bowey & Adamson (2002) suggest a shift from amorphous olivine-dominated grains in diffuse medium environments to amorphous pyroxenes in molecular clouds and young stellar objects (YSOs), indicating that some dust processing is occurring during the early stages of star formation. Further processing is evidenced by the presence of crystalline silicates in the dust surrounding some main-sequence stars, with amorphous olivine and forsterite as the dominant components (see, e.g., Knacke et al. 1993). Comets also contain both amorphous and crystalline silicates (see review by Wooden 2002), with crystalline fractions that are too high (up to 30% by mass) to be accounted for by the ISM (where the crystalline fraction is <2%; Kemper et al. 2004), indicating that crystallization occurred in the protosolar nebula.

Differences in the silicate spectra of interstellar versus solar system dust suggest an evolutionary sequence in which the grain composition changes from amorphous olivine to crystalline forsterite during the star and solar system formation process. Dust grains in accretion disks around young stars therefore must be significantly modified with respect to those of the ISM and are thus excellent laboratories for the study of in situ crystallization of silicates. If crystallization proceeds via annealing, then silicates in the outer disk are expected to accrete icy mantles and retain cores that are similar to ISM dust (i.e., amorphous olivine and pyroxene), while in the inner disk ($T \gtrsim 800$ K), microcrystalline lattice structures on 0.001 μm size scales can form within silicate grains (Gail 1998). If annealing continues for a sufficiently long time or occurs in a sufficiently hot environment, crystallization spreads from these critical nuclei over the entire grain. At disk radii corresponding to temperatures above $\sim$1000 K, 0.1–1 μm grains should be completely crystallized (Gail 1998) and larger dust grains should possess regions of localized crystallization detectable in IR spectra (Jaeger et al. 1994). Increases in temperature are also predicted to result in conversion from pyroxenes to olivines. Thus, we would expect both crystallization and composition (i.e., the content of Fe vs. Mg and olivine vs. pyroxene) of the silicates in disks to be dependent on exposure to stellar radiation (e.g., location in the disk, disk geometry, stellar type) and/or the duration of processing (e.g., amount of disk turbulence, disk age).

High spectral resolution studies of the warm dust emission near 10 μm are vital in understanding the composition and processing of dust in the planet-forming region (1–10 AU) of circumstellar disks around young stars. The dominant feature in the 8–13 μm spectral region accessible from the ground is from amorphous olivine (peaking at 9.7 μm), with weaker features arising from silica (SiO$_2$; 8.9 μm) and crystalline silicates including enstatite (MgSiO$_3$; 9.2 and 10.4 μm) and forsterite (Mg$_2$SiO$_4$; 10.2 and 11.3 μm).[6] The transition from amorphous olivine to crystalline forsterite results in a predicted shift of the silicate emission feature from 9.7 to 11.3 μm. However, analysis of the 10 μm silicate feature is complicated by the fact that the strength and shape of the emission cannot be uniquely correlated with abundance or composition. The presence of organics on grain surfaces results in increased opacity at $\lambda < 6$ μm and decreased contrast between the silicate band at 10 μm and

the adjacent continuum (D'Alessio et al. 2001). Grain size has a similar effect and for large grains ($a_{\mathrm{max}} > 10$ μm) the silicate bands disappear almost entirely (Wolf & Hillenbrand 2003). Additionally, Fabian et al. (2001) suggest that grain shape also needs to be taken into account in the interpretation of silicate spectra, particularly for strong crystalline bands, for which a combination of spherical and ellipsoidal grains may be required. Disk morphology and optical depth also influence the shape/strength of the silicate feature (Meeus et al. 2001; Bouwman et al. 2003). Despite difficulties in constructing unique interpretations, a number of ground- and space-based studies of the disks around T Tauri and Herbig Ae/Be (hereafter HAEBE) stars have been conducted, yielding important constraints on the evolution of circumstellar material.

Early studies of young low-mass stars (Cohen 1980; Cohen & Witteborn 1985; Wooden 1994; Hanner et al. 1995, 1998) show a single, rather sharp peak between 9 and 10 μm, resembling molecular clouds and the diffuse ISM. *Infrared Space Observatory* (*ISO*) spectra of young low-mass stars in Chameleon (Natta et al. 2000) display 10 μm silicate emission that is significantly broader and stronger than that from the diffuse ISM, but consistent with the emission predicted by a simple radiation transfer model of <1 μm amorphous pyroxene and/or olivine grains in a flared disk. More recent surveys (e.g., Sitko et al. 1999, 2000; Sylvester & Mannings 2000; Honda et al. 2003; Meeus et al. 2003; Przygodda et al. 2003; van Boekel et al. 2003), however, have found evidence in a few low-mass sources for a more trapezoidal shaped 8–13 μm amorphous silicate feature or even a pronounced 11.3 μm crystalline silicate (forsterite) bump, indicating that at least some dust processing has taken place in these objects.

HAEBE stars were studied more extensively with *ISO* and, based on 2–45 μm *ISO* spectra of HAEBE stars spanning a range of ages, an evolutionary sequence has been suggested (Meeus & Waelkens 1999). In this sequence, rising featureless dense cloud core spectra proceed to strong amorphous 10 μm silicate absorption from embedded protostars. These are followed by optically thick protoplanetary disks with spectra showing warm 10 μm silicate dust emission and prominent cold dust emission longward of 15 μm, then spectra with only warm dust interpreted as arising from disks undergoing planet formation, and finally the most evolved sources with nearly photospheric spectra, indicating disk dispersal. In addition to this general evolutionary trend, *ISO* detected crystalline silicate emission bands (11.3, 27.5, 33.5, 35.8, and 70 μm) toward a modest sample of HAEBE star+disk systems (Molster et al. 1999; Meeus et al. 2001). The longer wavelength emission bands are highly dependent on the structure of the dust. These studies show large variations in dust crystallinity and composition among YSOs of similar age and stellar properties (van den Ancker et al. 2000; Meeus et al. 2001), indicating the necessity of large samples to test scenarios of disk evolution.

Objects that may be in transition between primordial dust and debris dust (generated through collisions of planetesimals), or which are fully debris, have also been investigated (Sylvester et al. 1996; Sylvester & Mannings 2000), revealing generally photospheric or continuum excess spectra. The 10 μm spectrum of the 12^{+8}_{-4} Myr old (Zuckerman et al. 2001) A star β Pictoris, however, exhibits a remarkable resemblance to that of solar system grains and comets, suggesting a mixture of crystalline and amorphous material (Knacke et al. 1993; Reach et al. 2003). Direct imaging of β Pictoris shows a warped disk that is potentially caused by collisions of planetesimals and may be shaped by recent planet formation (Kalas & Jewitt 1995; Mouillet et al. 1997;

---

[6] The peak wavelengths described above correspond to the strongest features in the 8–13 μm region for 0.1 μm grains (Bouwman et al. 2001).

TABLE 1
Observations

Source	R.A. (J2000.0)	Decl. (J2000.0)	Observation Date	Reference Star	Aperture (pixels)	LSEC?
49 Cet..................................	01 34 37.78	−15 40 34.9	2000 Nov 8	α Tau	6	n
HD 17925	02 52 32.129	−12 46 10.972	2000 Feb 21	HR 1017	6	y
HD 22049	03 32 55.844	−09 27 29.744	2000 Dec 10	HR 1017	6	y
IRAS 04016+2610..............................	04 04 42.85	+26 18 56.3	2000 Dec 9	HR 617	6	y
IRAS 04108+2803B[a]..........................	04 13 52.9	+28 11 23	2000 Dec 10	HR 1017	6	y
IRAS 04169+2702..............................	04 19 59.24	+27 09 58.6	2000 Dec 10	HR 1017	6	y
IRAS 04181+2654A/B[a]........................	04 21 11.42	+27 01 08.9	2000 Dec 10	HR 531	6	y
IRAS 04239+2436..............................	04 26 57.1	+24 43 36	2000 Dec 10	HR 1017	6	y
IRAS 04248+2612..............................	04 27 56.7	+26 19 20	2000 Dec 9	HR 617	6	y
IRAS 04264+2433[a]..............................	04 29 07.68	+24 43 50.1	2000 Dec 9	HR 1017	6	y
Haro 6-10A	04 29 24.39	+24 33 02.1	2000 Dec 10	HR 1017	6	y
Haro 6-10B	04 29 24.39	+24 33 02.1	2000 Dec 10	HR 1017	6	y
IRAS 04287+1801..............................	04 31 33.6	+18 08 15	2000 Dec 9	HR 1708	6	y
IRAS 04295+2251..............................	04 32 32.07	+22 57 30.3	2000 Dec 9	HR 617	6	y
AA Tau..................................	04 34 55.2	+24 28 52	2000 Feb 21	HR 2990	6	y
IRAS 04325+2402[b]	04 35 33.0	+24 08 14	2000 Dec 9	. . .	. . .	. . .
LkCa 15[a].................................	04 39 17.8	+22 21 03	1999 Nov 30, 2000 Nov 8	α Aur	6, 3	n, n
IRAS 04381+2540[a]..............................	04 41 12.48	+25 46 37.1	2000 Dec 10	HR 531	6	y
IRAS 04489+3042[a]..............................	04 52 06.9	+30 47 17	2000 Feb 21	HR 1708	6	y
GM Aur[a]................................	04 55 10.2	+30 21 58	2000 Nov 8	α Tau	3	n
MWC 480...........................	04 58 46.27	+29 50 37.0	1999 Nov 30	α Tau	6	n
BN..	05 35 14.17	−05 22 23.1	2000 Dec 10	HR 2943	6	y
NGC 2024 IRS 2	05 41 45.8	−01 54 30	2000 Dec 10	HR 2943	6	y
Mon R2 IRS 3	06 07 47.8	−06 22 55	2000 Dec 10	HR 2943	6	y
HD 233517	08 22 46.71	+53 04 49.2	2000 Nov 8	α Aur	3	n
Hen 3-600A	11 10 27.9	−37 31 52	2000 Feb 21	HR 4786	6	y
HD 102647	11 49 03.578	+14 34 19.417	2000 Feb 19	HR 4534	6	y
HR 4796A	12 36 01.032	−39 52 10.219	2000 Feb 21	HR 4786	6	y
IRAS 14050−4109[a]..............................	14 05 05.7	−41 09 40	2000 Feb 21	HR 4786	6	y
HD 163296	17 56 21.29	−21 57 21.9	1999 Aug 23, 2000 Jun 20	β Oph	6, 3	n, y
HD 179218	19 11 11.254	+15 47 15.630	2000 Feb 21	HR 5908	6	y
WW Vul[a]..................................	19 25 58.75	+21 12 31.3	2000 Jun 20	ϵ Cyg	3	y
HD 184761	19 34 58.97	+27 13 31.2	2000 Nov 8	α Tau	3	n
HD 216803	22 56 24.0529	−31 33 56.042	2000 Dec 9	HR 1017	6	y

Note.—Units of right ascension are hours, minutes, and seconds, and units of declination are degrees, arcminutes, and arcseconds.
[a] Residuals of incomplete subtraction of the 9.7 μm telluric ozone feature are present in the spectrum.
[b] Photometric observations only. An 8−13 μm spectrum was not acquired for this source.

Augereau et al. 2001). Spatially resolved 10 μm spectroscopy of β Pictoris (Weinberger et al. 2003) revealed that the silicate emission arises only from dust within 20 AU of the star, compared to the 77 AU emitting region in the continuum. Furthermore, the mixture of amorphous and crystalline dust appears to remain constant, suggesting that the crystallization process may be acting uniformly as a function of radius within the planet formation region.

Observations of silicate emission toward YSOs in a variety of evolutionary stages can provide valuable information about the modification of dust during solar system formation. In the present study, 8−13 μm spectra were obtained for 34 low- and intermediate-mass young stars, ranging from embedded protostars to debris disk systems. Additional photometry at 10.7 μm was obtained for a subset of the sample in order to facilitate flux calibration of the spectra. In § 2 the sample selection criteria are discussed. The spectroscopic and photometric observations and data reduction are described in § 3. Spectral energy distributions (SEDs) compiled from the literature are presented in § 4, along with implications regarding the evolutionary categories within the sample. In § 5 the 8−13 μm spectra are discussed qualitatively, and in § 6 a quantitative analysis of the silicate emission spectra is presented. Conclu-

sions and suggestions of future work are discussed in § 7. The appendices contain the references for the SEDs (Appendix A) and a short discussion of variability in the silicate feature (Appendix B).

2. SAMPLE SELECTION

Spectra in the 10 μm region of a moderate sample of optically visible HAEBE stars, T Tauri stars, and more heavily embedded YSOs were acquired. The goal was to use the spectra to characterize the composition of the dust, particularly the degree of crystallinity of the silicate grains present. Objects with varying age and mass were chosen in order to put this information in context with the stellar evolutionary process for both low- and high-mass stars. The sample includes seven low-mass class I objects chosen from Kenyon et al. (1993) and three well-known high-mass YSOs: the Becklin Neugebauer object (BN), NGC 2024 IRS 2, and Mon R2 IRS 3. These observations probe the composition of largely unprocessed grains, and absorption from amorphous silicates is expected. There are 10 optically visible class II T Tauri and HAEBE stars in the sample, most of which have very well characterized SEDs. *ISO* observations indicate that at least two HAEBE stars in this intermediate-age sample, HD 163296 and HD 179218, possess detectable amounts of

TABLE 2
Flux Calibration of Spectra

Source	λ (μm)	Flux (Jy)	$\Delta\lambda$ (μm)	Instrument	References
49 Cet..................................	10.8	0.20 ± 0.04	8.0–13.6	Keck II, OSCIR	1
HD 17925	10.7	0.92 ± 0.09	10.0–11.4	Keck, LWS	2
HD 22049	12	9.5 ± 0.4	9.15–14.85	*IRAS*	3
IRAS 04016+2610[a].................	10.7	2.8 ± 0.2	10.0–11.4	Keck, LWS	4
	10.3	2.5 ± 0.1	9.65–10.95	IRTF	5
IRAS 04108+2803B[a].................	10.7	1 ± 3	10.0–11.4	Keck, LWS	4
	10.3	0.57 ± 0.09	9.65–10.95	IRTF	5
IRAS 04169+2702......................	12.0	0.75 ± 0.05	9.15–14.85	*IRAS*	3
IRAS 04181+2654A/B	12.0	0.36 ± 0.05	9.15–14.85	*IRAS*	3
IRAS 04239+2436......................	12.0	1.71 ± 0.09	9.15–14.85	*IRAS*	3
IRAS 04248+2612......................	10.7	0.230 ± 0.009	10.0–11.4	Keck, LWS	4
IRAS 04264+2433......................	10.7	0.41 ± 0.02	10.0–11.4	Keck, LWS	4
Haro 6-10A	10.0	4.3[b]	. . .	. . .	6
Haro 6-10B	10.3	10 ± 2	9.65–10.95	IRTF	5
IRAS 04287+1801......................	10.7	5.0 ± 0.4	10.0–11.4	Keck, LWS	4
IRAS 04295+2251......................	10.7	0.69 ± 0.03	10.0–11.4	Keck, LWS	4
AA Tau.....................................	10.7	0.44 ± 0.03	10.0–11.4	Keck, LWS	2
IRAS 04325+2402[c]......................	10.7	0.060 ± 0.003	10.0–11.4	Keck, LWS	4
LkCa 15	9.6	0.50 ± 0.15	9.5–9.7	*ISO*, SWS	7
IRAS 04381+2540......................	10.1	0.23 ± 0.05	9.65–10.95	IRTF	5
IRAS 04489+3042......................	10.7	0.31 ± 0.02	10.0–11.4	Keck, LWS	4
GM Aur.....................................	10.1	0.5	7.55–12.65	IRTF	8
MWC 480	9.6	8.7 ± 2.6	9.5–9.7	*ISO*, SWS	7
BN..	10.7	88	10.0–11.4	Keck, LWS	4
NGC 2024 IRS 2	10.5	19 ±1	8.0–13.0	MANIAC, ESO	9
Mon R2 IRS 3	10.0	165 ±5	9.65–10.95	IRTF	10
HD 233517	10.1	0.439	9.595–10.505	UKIRT, Berkcam	11
Hen 3-600A...............................	10.7	0.73 ± 0.06	10.0–11.4	Keck, LWS	2
HD 102647	10.7	5.51 ± 0.41	10.0–11.4	Keck, LWS	2
HR 4796A.................................	10.7	0.22 ± 0.02	10.0–11.4	Keck, LWS	2
IRAS 14050−4109......................	10.7	0.23 ± 0.02	10.0–11.4	Keck, LWS	2
HD 163296	9.69	18.6 ± 0.5	8.84–10.54	1 m, ESO	12
HD 179218	10.7	17 ± 2	10.15–11.25	O'Brien, bolometer	13
WW Vul.....................................	9.6	2.3 ± 0.5	9.5–9.7	*ISO*, SWS	7
HD 184761	12	2.41	9.15–14.85	*IRAS*	3
HD 216803	10.7	1.53 ± 0.082	10.0–11.4	Keck, LWS	2

[a] Photometric errors are larger in the data acquired in this study; therefore, 10.3 μm photometry from Myers et al. (1987) was used for flux calibration.

[b] Flux for Haro 6-10B is an estimate by Leinert & Haas (1989).

[c] Photometric observations only. An 8–13 μm spectrum was not acquired for this source.

References.—(1) Jayawardhana et al. 2001; (2) Metchev et al. 2004; (3) Beichman et al. 1988; (4) this paper; (5) Myers et al. 1987; (6) extrapolation from Leinert & Haas 1989; (7) Thi et al. 2001; (8) Kenyon et al. 1993; (9) Walsh et al. 2001; (10) Koresko et al. 1993; (11) Skinner et al. 1995; (12) Berrilli et al. 1992; (13) Lawrence et al. 1990.

crystalline silicates (van den Ancker et al. 2000; Meeus et al. 2001). Seven older main-sequence stars with debris disks were also included, which possess optically thin IR continua and ages older than 6 Myr. These are the most likely candidates for detection of crystalline silicates, provided that warm dust is present. Our source list and observing dates are provided in Table 1.

3. PHOTOMETRIC AND SPECTROSCOPIC OBSERVATIONS

The 8–13 μm spectra/photometry were obtained using the Long Wavelength Spectrometer (LWS) at the W. M. Keck Observatory between 1999 August and 2000 December (see Table 1). LWS provides diffraction-limited (FWHM = 0″.22) imaging (10″ field of view, 0″.08 pixel^{-1}) and long-slit (7″) spectroscopic ($R = 100$–1400) capabilities in the 3–25 μm wavelength range. Photometry was obtained with the 10.7 μm filter ($\Delta\lambda = 10.0$–11.4 μm) for sources observed during the

nights of 2000 February 20–21 and December 9, under poor and variable seeing conditions: 0″.3–0″.6 at 10 μm. The Nwide filter and low-resolution grating (LRES) were used to obtain 8–13 μm spectra, with $R = 100$, at a dispersion of 0.037 μm pixel^{-1}. Slit widths of 3 and 6 pixels were used, resulting in 0″.24 and 0″.48 apertures, respectively. Sources were imaged prior to each spectroscopic observation to ensure optimal placement within the slit. For most spectroscopic observations, additional calibration scans were obtained using the Keck routine LSEC, in which the data are chopped between an ambient blackbody source ($T \approx 274$ K) and the sky. Darks were taken at the end of each night with exposure times equal to those on source. The raw "six-dimensional" LWS data, consisting of images for two chop-nod pairs, were co-added into two-dimensional images, using the IDL routine *lwscoadd*.[7]

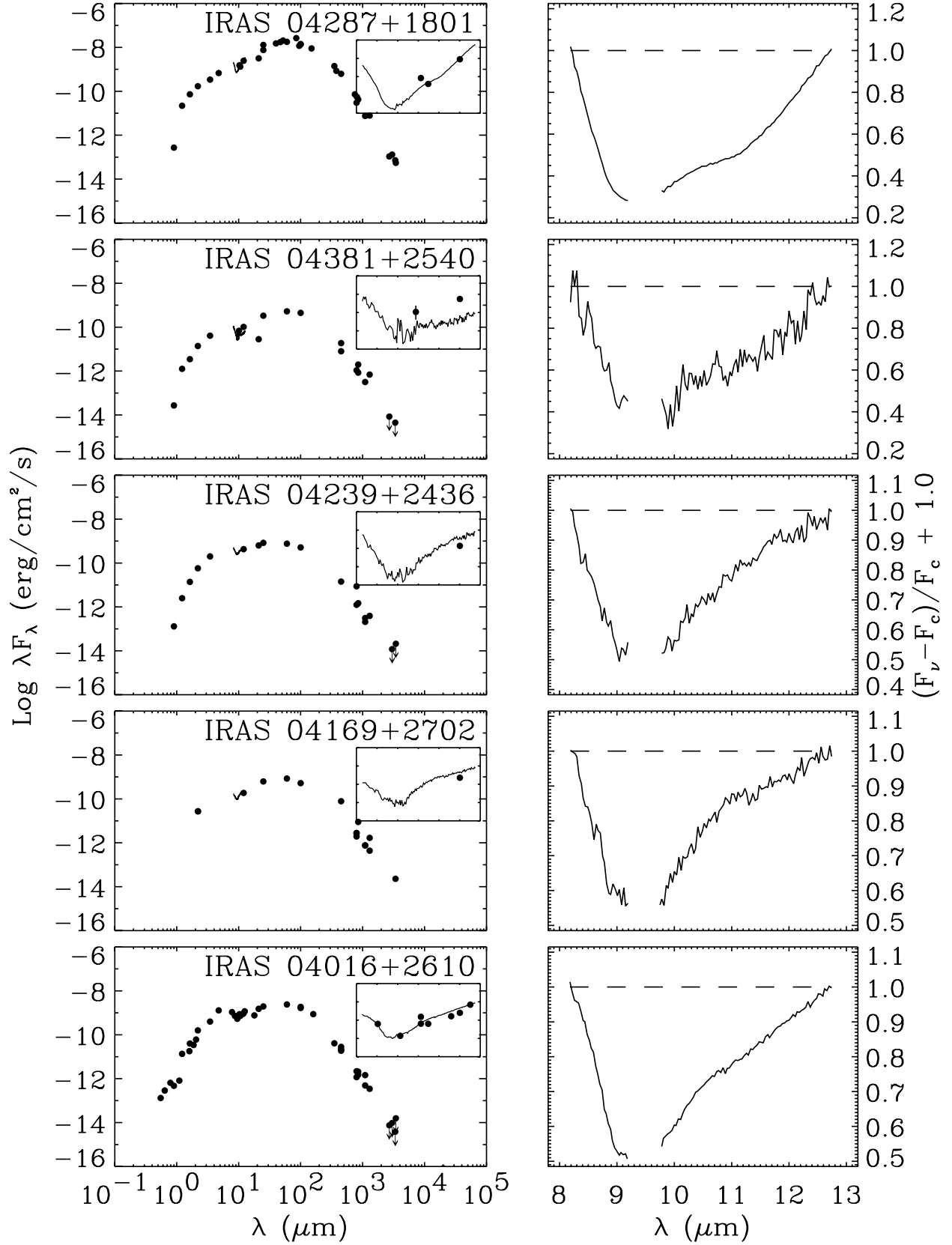[7] The *lwscoadd* routine was written by Gregory D. Wirth and is provided by the observatory at http://www2.keck.hawaii.edu/inst/lws/lwscoadd.html.

FIG. 1.—SEDs and 10 μm spectra for low-mass stars where silicates are in absorption. The left panels display the SEDs for each source (see Appendix A for references) in units of log (λF_λ), with the 10 μm spectra included for reference. The insets show enlargements of the 8–13 μm regions with linear scaling on both axes. Open symbols are data for which a single source within a binary or multiple cannot be distinguished. The continuum is in most (but not all) cases adequately represented by connecting the two end points of the spectrum, and normalized spectra are shown in the right panels in units of $(F_\nu - F_c)/F_c$ (see text for details). The dashed line depicts the continuum level.
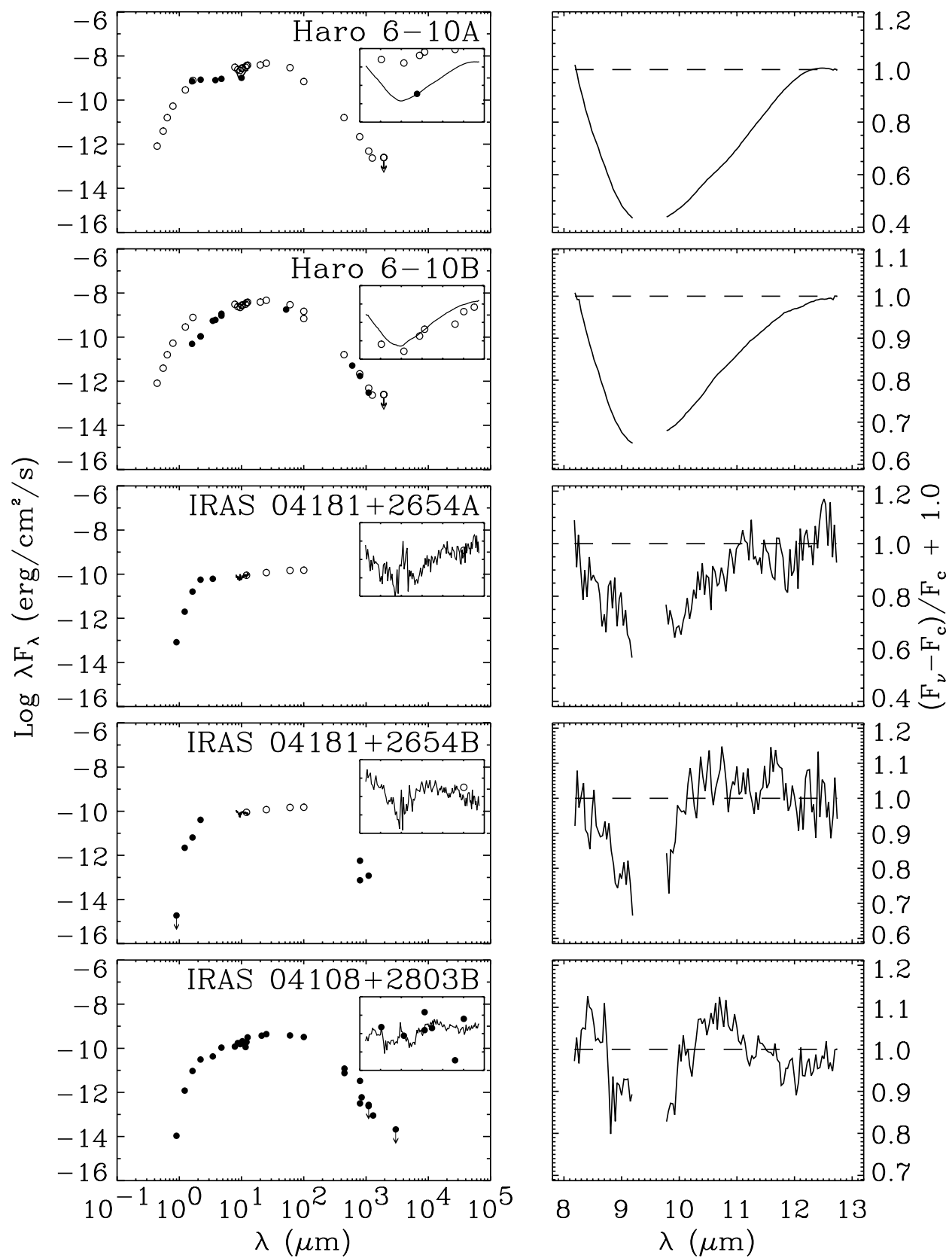
FIG. 1.—*Continued*
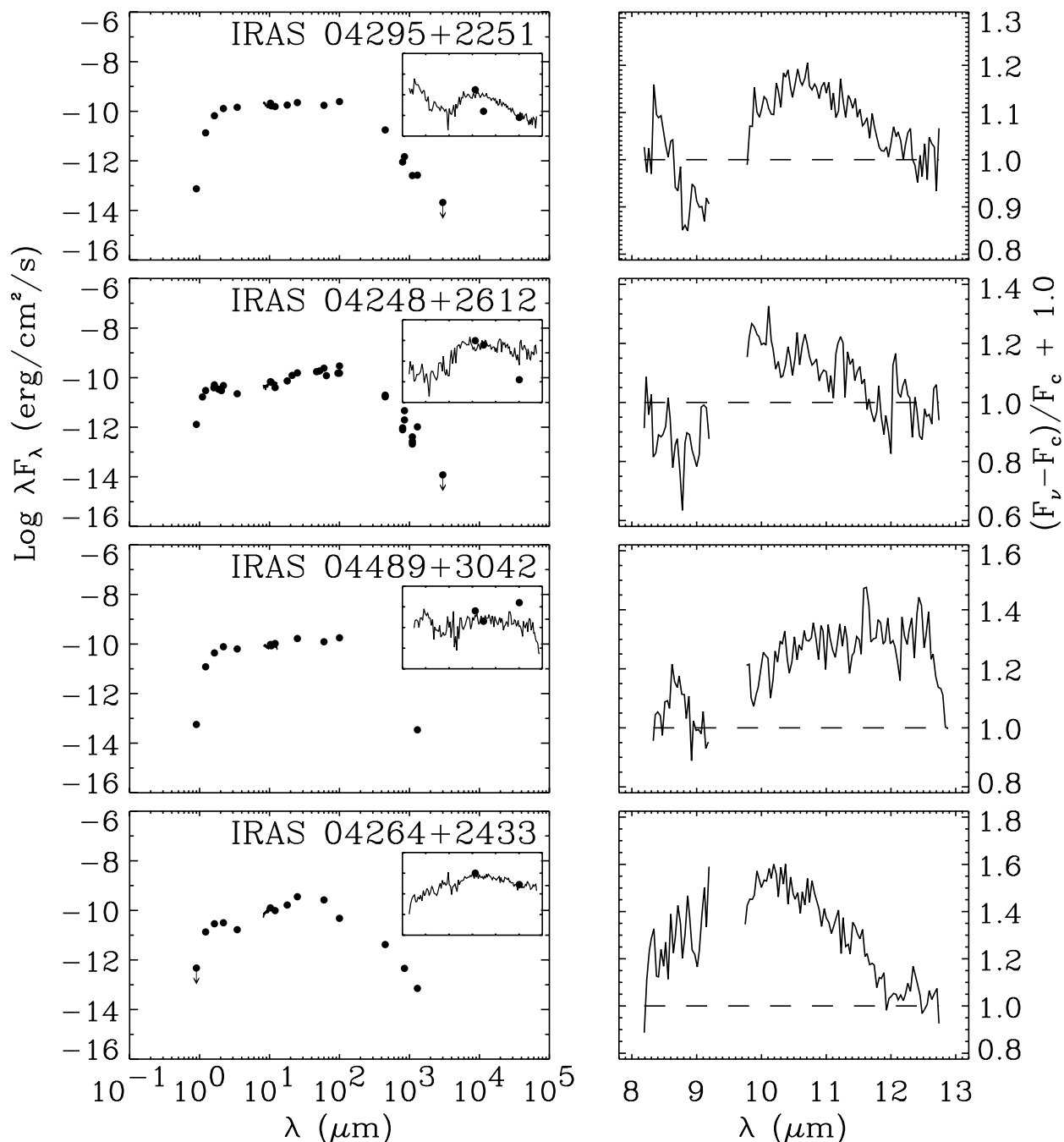
Fig. 1.—*Continued*

The IRAF *phot* task was used for the photometric data reduction. Apertures of radius 0″.96 (12 pixels) were used for the photometry and the sky background was measured in 2″.0–3″.2 radius (25–40 pix) annuli. Flat-fielding was found to increase the scatter in the photometry and therefore not performed. A curve-of-growth correction of −0.12 ± 0.01 mag (based on standard-star measurements) to a 1″.92 (24 pixel diameter) aperture was applied to each star, resulting in magnitudes within ~5% of the infinite aperture value. Standard-star observations were used to obtain extinction curves for each night. We derived a typical night-to-night variation in the atmospheric zero points of ~20% and an average atmospheric extinction correction of −0.32 ± 0.07 mag per air mass. The

rms scatter in the photometry of the standards is 0.06 mag for 2000 February 20 and 21 and 0.13 mag for 2000 December 9.

The spectroscopic data reduction was performed using the NOAO IRAF TWODSPEC and ONEDSPEC packages. After applying pixel masks and flat fields, the images were then divided by those produced from the LSEC calibration scan obtained closest in time to the observation, to correct for variations in the spectral response of the grating. The detector's dark current was found to be negligible over the integration times used and therefore not subtracted from the data. Spectral extraction was performed via standard methods using the IRAF task *apall*. For the purposes of wavelength calibration and removal of the telluric ozone absorption feature at ~9.5 μm, each
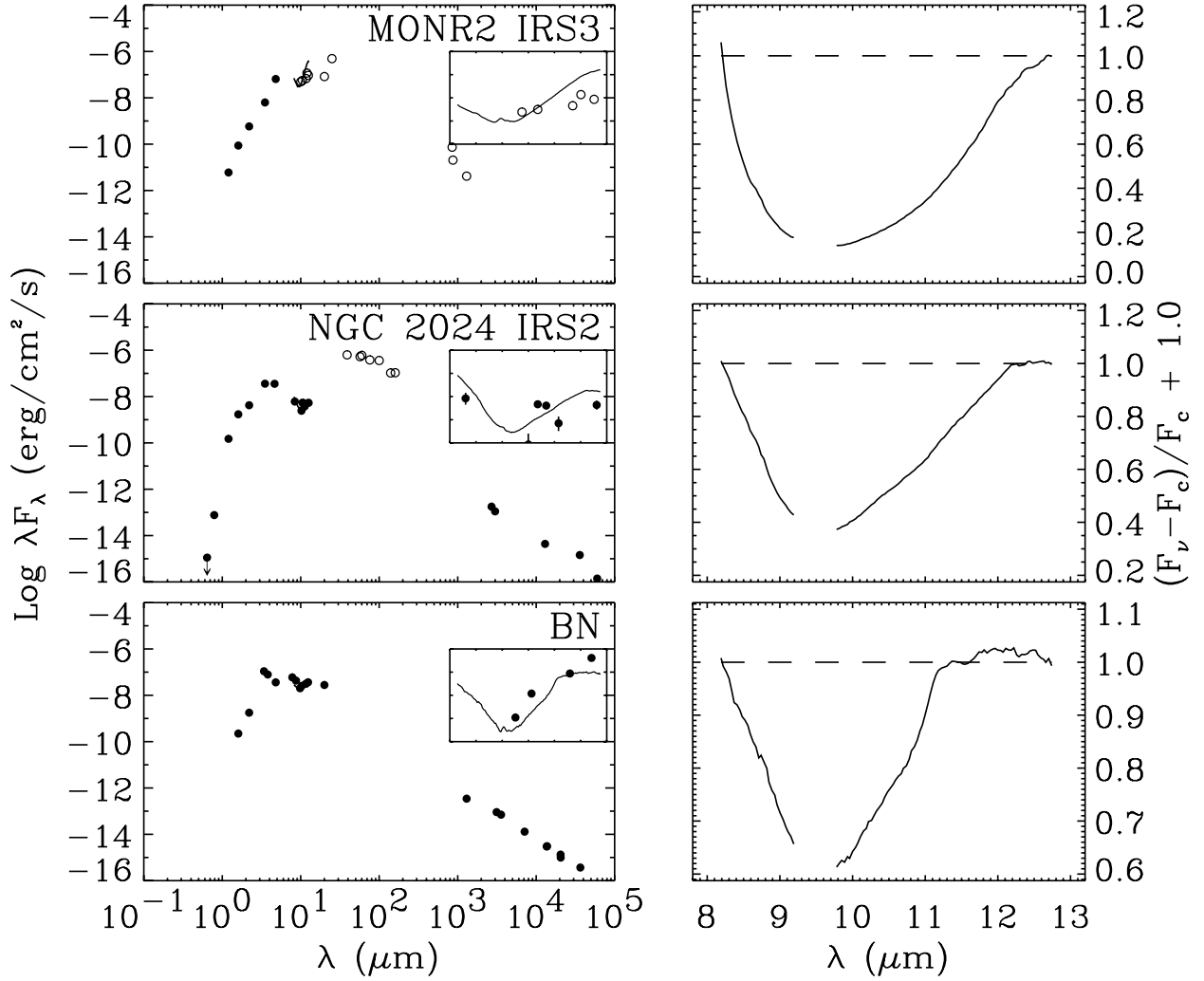
Fig. 2.—Same as Fig. 1, but for SEDs and 10 μm spectra for high-mass stars where silicates are in absorption.

extracted spectrum was aligned with and divided by a standard-star spectrum (see Table 1 for details) using the IRAF *telluric* task. In some cases (as noted in Table 1), variations in seeing and atmospheric transmission versus wavelength resulted in small differences in the shape of the telluric ozone absorption feature observed in the target and calibrator spectra, and residuals can be seen in the resulting divisions. After telluric corrections were performed, the resulting spectra were multiplied by a blackbody emission spectrum appropriate to each calibrator to remove any induced slope in the 8–13 μm region. Absolute flux calibration was performed using photometric observations at similar wavelengths culled from the literature or obtained in this study (as indicated in Table 2), with scale factors obtained from the spectrum integrated over the photometric bandwidth. Flux-calibrated spectra are shown in Figures 1–6. The spectra are overplotted onto the SEDs to indicate the success of this flux calibration method.

4. SPECTRAL ENERGY DISTRIBUTIONS

Continuum fluxes for the sources in our sample were collected from the literature in order to form the SEDs shown in Figures 1–6. The data were not dereddened, but, as the A_V for all but the class I sources is small (<3 mag), this should have a modest effect on fluxes for wavelengths longer than 1.2 μm (*J* band). In Figures 3–6, the SEDs for stars with known spectral types are overlaid with emission arising from a blackbody at the stellar temperature found in the literature for each source (see Table 3) by scaling the peak of the blackbody curve to match the SED at that wavelength. More quantitatively, stellar luminosities were found by calculating a color excess and A_v for the given spectral type, applying a bolometric correction to the *V* or *I* magnitude (as indicated), and converting to bolometric luminosity using the given distance (see Table 3 for details). For comparison, stellar luminosities from the literature are also presented. These are similar to the luminosities derived here; a notable exception is HD 179218, for which the *V*-band magnitudes reported in the literature vary by up to 1.3 mag. For consistency, we use the luminosities derived here but note that there may be errors for stars with large variability.

The IR luminosity and the ratio L_{IR}/L_* (indicative of dust geometry for optically thick disks and of midplane optical depth for optically thin disks) were estimated from the SEDs collected for our sample in the following manner. First, the wavelength (λ_{onset}) at which the photometric flux is greater than twice that of the stellar blackbody was evaluated.[8] The infrared luminosity of the disk L_{IR} was then calculated by integrating the SED

---

[8] Parameter λ_{onset} is calculated to give the reader an impression of where the SED begins to deviate from photospheric and was chosen to be the point at which the photometric flux is greater than *twice* that of the stellar blackbody as this minimizes the errors due to variability in the photometric measurements.
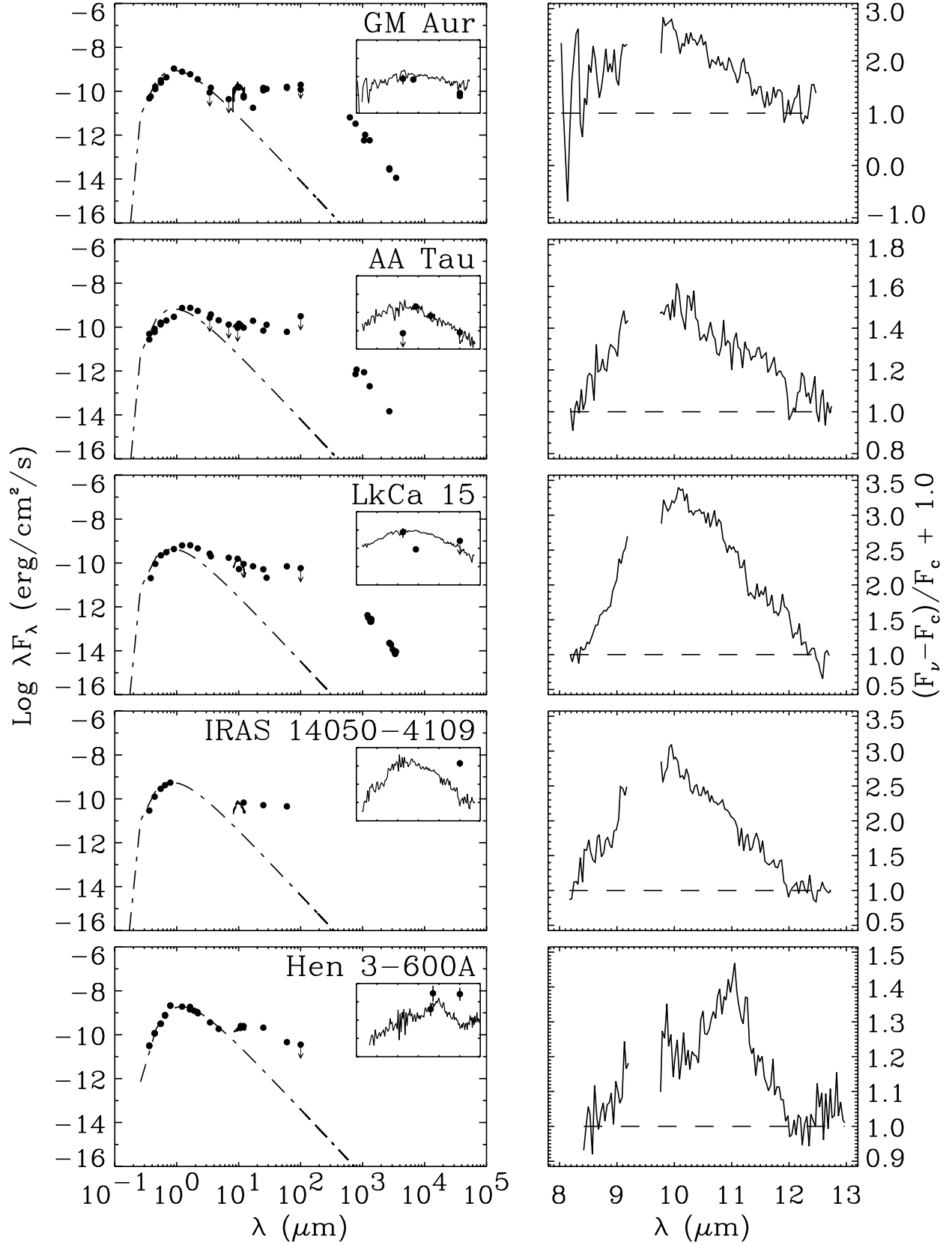
FIG. 3.—SEDs and 10 μm spectra for disks around low-mass T Tauri stars where the silicate 10 μm band is in emission. In the left panels, the SEDs are plotted in units of $\log(\lambda F_\lambda)$ overlaid by dashed lines representing the stellar photosphere, as fitted by the blackbody model described in the text. The insets show an enlargement of the 8–13 μm region with linear scaling on both axes. The continuum is obtained by connecting the two end points of the spectrum. Continuum-subtracted spectra in units of $(F_\nu - F_c)/F_c$ are shown in the right panels, with the continuum level depicted by dashed lines.
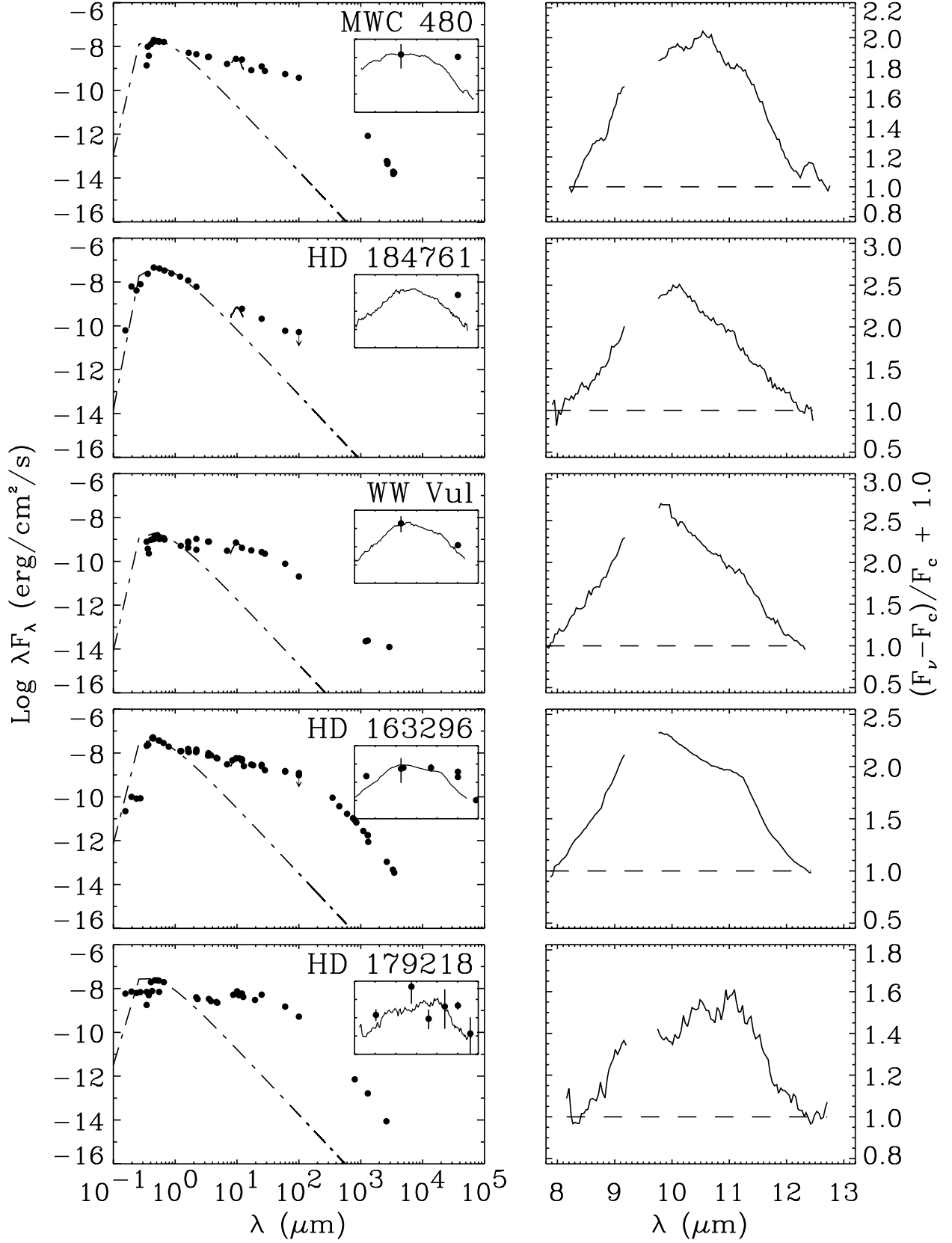
FIG. 4.—Same as Fig. 3, but for SEDs and 10 μm spectra for disks around intermediate-mass HAEBE stars where the silicate 10 μm band is in emission.
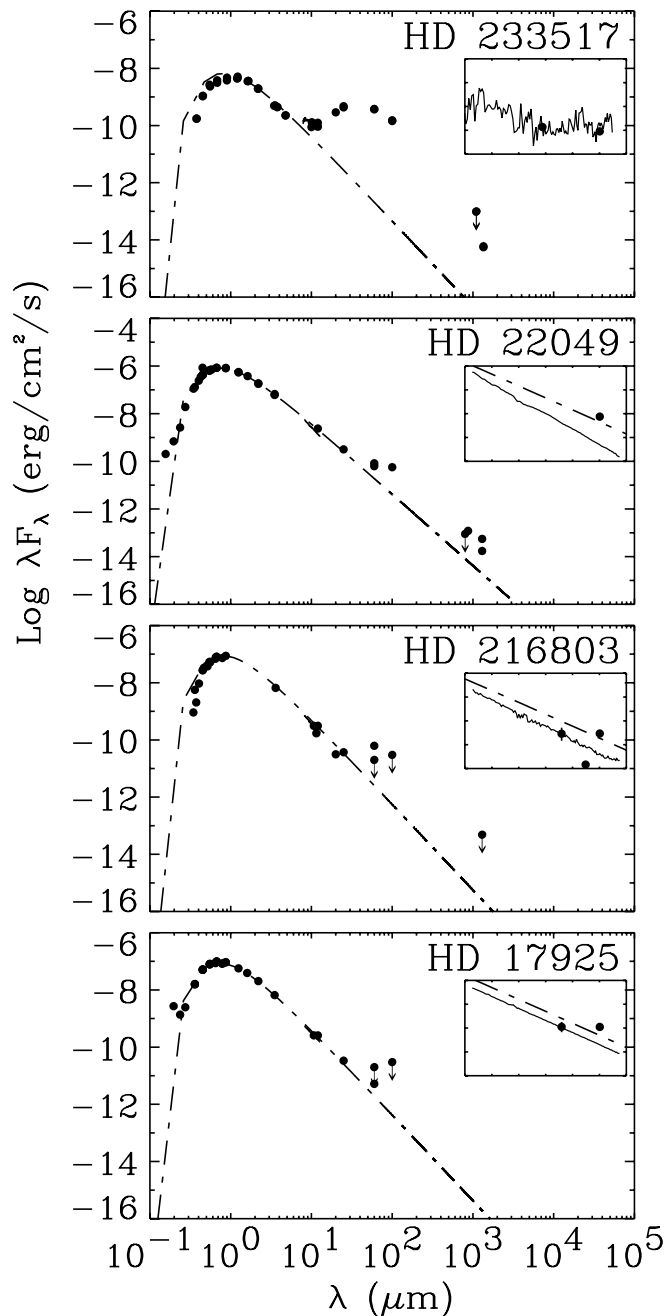
FIG. 5.—SEDs including 10 μm spectra for "debris" disks around low-mass stars. Dashed lines represent the stellar photosphere. The insets show an enlargement of the 8–13 μm region with linear scaling on both axes.

FIG. 6.—Same as Fig. 5, but for SEDs including 10 μm spectra for "debris" disks around intermediate-mass stars.

between λ_{onset} and 1 cm and subtracting the integral of the stellar blackbody over the same region. The resulting IR-to-stellar luminosity ratios (L_{IR}/L_*), as well as the wavelengths of the onset of excess radiation (λ_{onset}), are presented in Table 3. As the spectral types and A_V for the embedded YSOs are uncertain, only total luminosities were calculated; resulting values of L_{tot} are presented in Table 4.

The SEDs were used to establish the continuum around the 8–13 μm silicate emission feature, which is extremely important for analysis of the feature shape and the silicate composition. To establish the continuum for HAEBE stars, van Boekel et al. (2003) fitted each SED with a blackbody for the star and several blackbodies of different temperatures for the dust emission and interpolated between the two. Natta et al. (2000) fitted
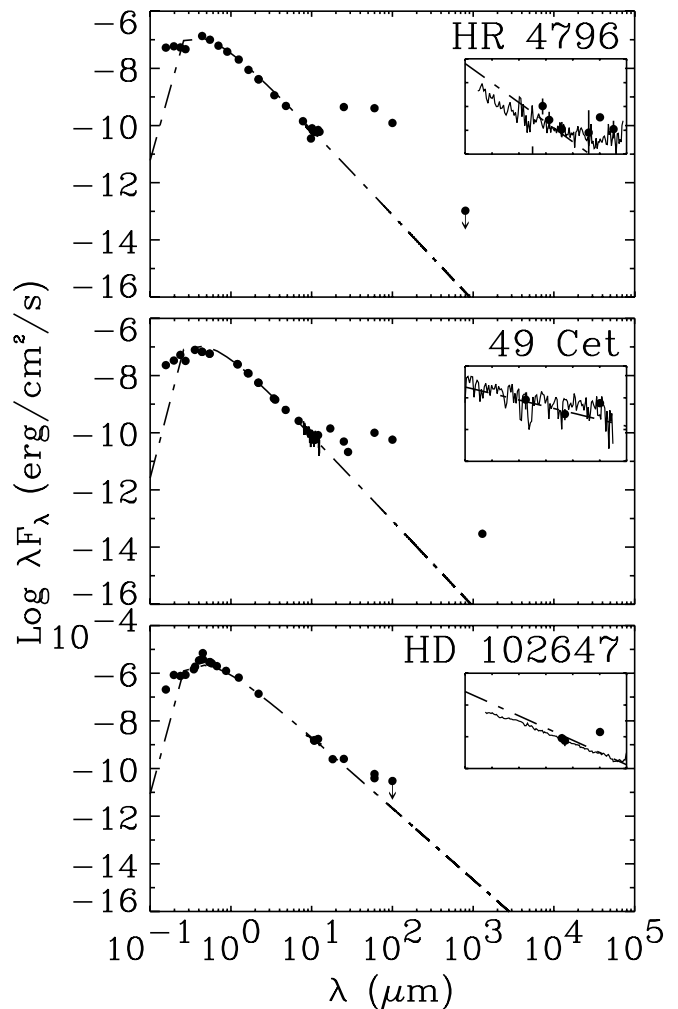
a power law to the edges of the silicate emission feature to remove the continuum in a sample of T Tauri stars. Upon examination of the overlays of the spectra on the SEDs in Figures 3 and 4, we find that for our sample the continuum is adequately represented by connecting the two end points of the spectrum (averaging over 0.20 μm near 8.3 and 12.2 μm).

In general, we would expect the shape of the 8–13 μm feature to be related to the SED and to the relative disk versus stellar radiation. Specifically, if changes in the silicate feature are due to processing of the dust, through growth and/or crystallization, then the shape of the silicate emission feature should be related to the evolutionary stage of the source. Because the spectral index is an indicator of the evolutionary class, we expect that it may be related to the shape of the 8–13 μm spectra. In the following sections we explore these trends, first through qualitative discussion and then through quantitative characterization of the spectral strength and shape.

5. DISCUSSION OF THE 10 μm SPECTRA

The flux-calibrated $0.1–10^5$ μm SEDs and 8–13 μm spectra are shown in Figures 1–6, with the continuum-subtracted silicate features shown in the right panels of Figures 1–4. The sources are placed into categories based on the shape of the SEDs and 8–13 μm spectra. In general, the debris disks are found to have little or no evidence of silicate emission, the

TABLE 3
STELLAR PARAMETERS FROM THE LITERATURE AND CALCULATIONS FROM SEDs: REVEALED DISKS

Source	Distance (pc)	Spectral Type	L_* ($L_\odot$)	T_{eff} (K)	Age (Myr)	References[a]	Method[b]	A_v[c]	$L_{*,\mathrm{bol}}$[d] ($L_\odot$)	λ_{onset}[e] (μm)	L_{IR}/L_*[f]	Spectral Index[g]
49 Cet........................	61	A1 V	23.44	9500	7.8	1, 2	$V/B-V$	0.21	22	25	1.1 (−3)	1.94
HD 17925	10.4	K1 V	...	5000	80	3	$V/B-V$	0	0.43	60	<6.0 (−5)	2.64
HD 22049	3.2	K2 V	...	5000	330	3	$V/B-V$	0	0.33	60	9.7 (−5)	2.61
AA Tau......................	140	K7	0.71	4060	2.4	2, 4	$I/V-I$	1.0	0.60	2.2	0.48	0.84
LkCa 15	140	K5: V	0.74	4350	2.0	2, 5	$I/V-I$	1.1	0.86	1.2	0.49	0.90
GM Aur......................	140	K7	0.724	4060	1.8	2, 4	$J/J-H$[h]	0.06	0.73	6.9	0.43	0.48
MWC 480[i]	131–140	A3 e	11–32	8460–8890	4.6	6, 7	$V/B-V$	0.25	14	1.6	0.29	0.53
HD 233517	23	K2	0.20	4500	...	8	$I/V-I$	0.30	0.12	10	0.12	0.62
Hen 3-600A	50.0	M4	...	3290	10.0	9	$I/V-I$	0.10	0.43	11	9.1 (−3)	0.62
HD 102647	11.1	A3 V	...	8590	240	3	$V/B-V$	0	14	60	<3.9 (−6)	2.59
HR 4796A..................	76	A0 V	35	10000	8.0	10, 11	$I/V-I$	0	26	25	4.6 (−3)	0.92
IRAS 14050−4109....	140	K5	...	4405	...	12	$I/V-I$	0.81	0.78	12	8.6 (−2)[j]	0.68
HD 163296	122^{+17}_{-13}	A1 Ve	30.2	9332	4.0	6	$V/B-V$	0.34	32	1.2	0.28	0.58
HD 179218	240^{+70}_{-40}	B9 e	316	10471	0.1	6	$V/B-V$	0.59	110	2.2	0.32	0.13
WW Vul.....................	550	A3 e/B9 V	43	8600	...	13	$V/B-V$	0.95	30	1.6	0.50	0.57
HD 184761	65	A8 V	...	7500	...	14	$V/B-V$	0.09	7.4	2.2	0.10	1.38
HD 216803	7.70	K5 Ve	...	4555	200	15, 16	$V/B-V$	0.06	0.20	60	<7.0 (−4)	2.67

NOTE.—Parameters in the columns to the left of the References column are from the literature as noted; those on the right are calculated here.

[a] Where two references are listed, the second is for the age.

[b] Method is in the form of $A/B-C$, where $B-C$ is the color used to calculate the stellar A_v and A is the band to which the bolometric correction was applied.

[c] Values of A_v were calculated from the spectral type given and color excess $E(B-C)$, as defined in the Method column.

[d] Stellar bolometric luminosities were calculated by applying a bolometric correction to the magnitude of band A (defined in the Method column) and converting to luminosity using the given distance.

[e] Parameter λ_{onset} is the wavelength at which the stellar blackbody and a polynomial fit to the SED diverge.

[f] Parameter L_{IR} is calculated by integrating the SED between λ_{onset} and 1 cm and subtracting the integral of the stellar blackbody over the same region; $L_* = L_{*,\mathrm{bol}}$.

[g] The spectral indices are calculated following the method of Kenyon & Hartmann (1995), spectral index $= -[\log(\lambda_b F_{\lambda_b}) - \log(\lambda_a F_{\lambda_a})]/[\log(\lambda_b) - \log(\lambda_a)]$; $\lambda_a \approx 2.2$ μm for most sources, excepting IRAS 14050−4109 (0.8 μm) and HD 216803 (3.6 μm); $\lambda_b = 25$ μm for all sources.

[h] J- and H-band data were used to calculate the luminosity for GM Aur, as the I-band magnitude seemed anomalously high.

[i] Values of $d = 131$ pc and $T_{\mathrm{eff}} = 8710$ were used for the luminosity calculations for MWC 480.

[j] The SED for IRAS 14050−4109 could not be extrapolated beyond the last observed point (100 μm); therefore, this luminosity ratio is a lower limit.

REFERENCES.—(1) Coulson et al. 1998; (2) Thi et al. 2001; (3) Habing et al. 2001; (4) Hartmann et al. 1998; (5) Strom et al. 1989; (6) van den Ancker et al. 1998; (7) Simon et al. 2000; (8) Skinner et al. 1995; (9) Torres et al. 2003; (10) Jura et al. 1993; (11) Stauffer et al. 1995; (12) Gregorio-Hetem & Hetem 2002; (13) Natta et al. 2001; (14) Miroshnichenko et al. 1999; (15) Barrado y Navascues et al. 1997; (16) Santos et al. 2004.

TABLE 4
CALCULATIONS FROM SEDs: EMBEDDED OBJECTS

Source	L_{tot}	Distance (pc)	References	Spectral Index[a]
IRAS 04016+2610.......	3.7	140	1	−1.03
IRAS 04108+2803B	0.75	140	1	−1.09
IRAS 04169+2702.......	1.20	140	2	−1.29
IRAS 04181+2654A	0.34	140	1, 3	−0.31
IRAS 04181+2654B	0.34	140	1, 3	−0.44
IRAS 04239+2436.......	1.39	140	1	−1.10
IRAS 04248+2612.......	0.10	140	1	−0.49
IRAS 04264+2433.......	0.24	140	1	−1.00
Haro 6-10A	6.5	140	2	−0.71
Haro 6-10B	6.5	140	2	−1.56
IRAS 04287+1801.......	0.29	140	1	−1.78
IRAS 04295+2251.......	0.41	140	1, 3	−0.23
IRAS 04381+2540.......	0.70	140	3	−1.31
IRAS 04489+3042.......	0.31	140	1	−0.31
BN...............................	980	450	4	−1.25
NGC 2024 IRS 2.........	5800	415	5	−1.74
Mon R2 IRS 3.............	30000	830	6	−2.77

NOTE.—The luminosities for several close sources are those of the combined sources as a result of the large IRAS beam.

[a] The spectral indices are calculated as in Table 3; $\lambda_a = 2.2$ μm for all sources; $\lambda_b = 25$ μm for all low-mass stars and 20, 25, and 39 μm for BN, NGC 2024 IRS 2, and Mon R2 IRS 3, respectively.

REFERENCES.—(1) Hartmann 2002; (2) Myers et al. 1987; (3) Beichman et al. 1988; (4) Gezari et al. 1998; (5) Haisch et al. 2001; (6) Preibisch et al. 2002.

T Tauri and HAEBE sources show strong to moderate silicate emission, and the embedded sources show silicate absorption, or a combination of absorption and emission. Possible evolutionary trends are shown in Figures 7 and 8 for the low-mass and intermediate-mass stars, respectively. The trend shown in Figure 8 is similar to that suggested for HAEBE stars by Meeus & Waelkens (1999). The evolution of low-mass star spectra and SEDs does not appear to be significantly different from intermediate-mass stars, with embedded sources showing amorphous olivine in absorption, followed by stages of dust processing (including grain growth and/or silicate crystallization) resulting in variations in the shape of the emission feature, and finally photospheric spectra for debris disks. One possible difference between the low- and intermediate-mass stars in our sample is that for the intermediate-mass stars, crystalline silicates have been found in sources that possess large near- and far-IR excesses, but the one low-mass star toward which crystalline silicates have been found, Hen 3-600A (see also Honda et al. 2003; Uchida et al. 2004), has an SED with no near-IR excess and diminishing far-IR flux. In addition, there have been far fewer detections of crystalline silicates toward low-mass (with respect to high-mass) stars reported in the literature. It is not at all clear, however, that the surveys to date are drawn from representative samples.

5.1. Silicate Absorption Spectra

The silicate feature is clearly seen in absorption in nine low-mass embedded sources and in all three high-mass protostars in
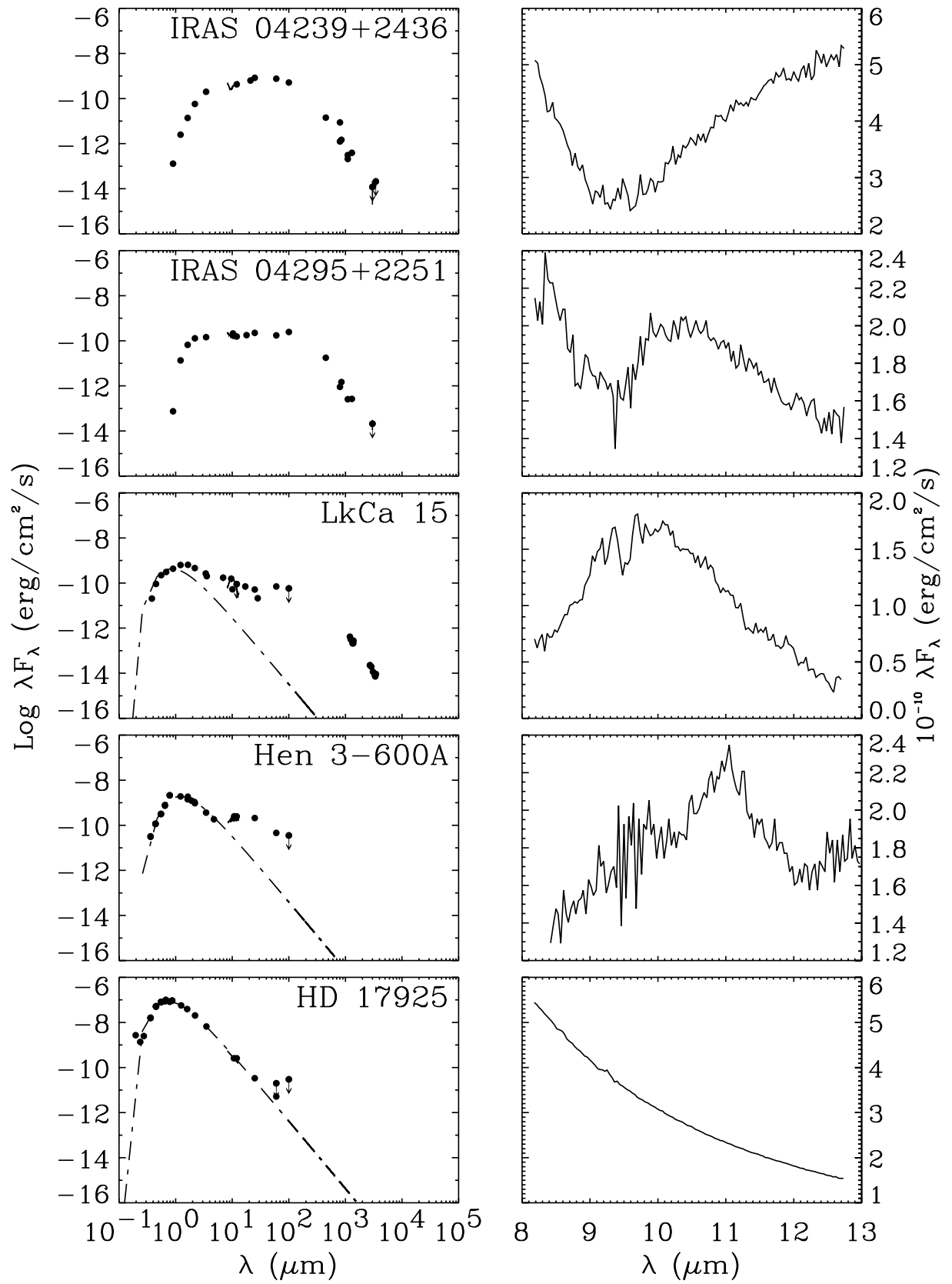
Fig. 7.—Evolution of the silicate spectrum for low-mass stars. The left panels display the SEDs for selected sources in units of $\log(\lambda F_\lambda)$, with the 10 μm spectra included for reference. The right panels show an enlargement of the 8–13 μm region with linear scaling on both axes. Symbols and lines are as described in Figs. 1–6. The evolutionary sequence for low-mass stars is quite similar to that for intermediate-mass stars (Meeus & Waelkens 1999).
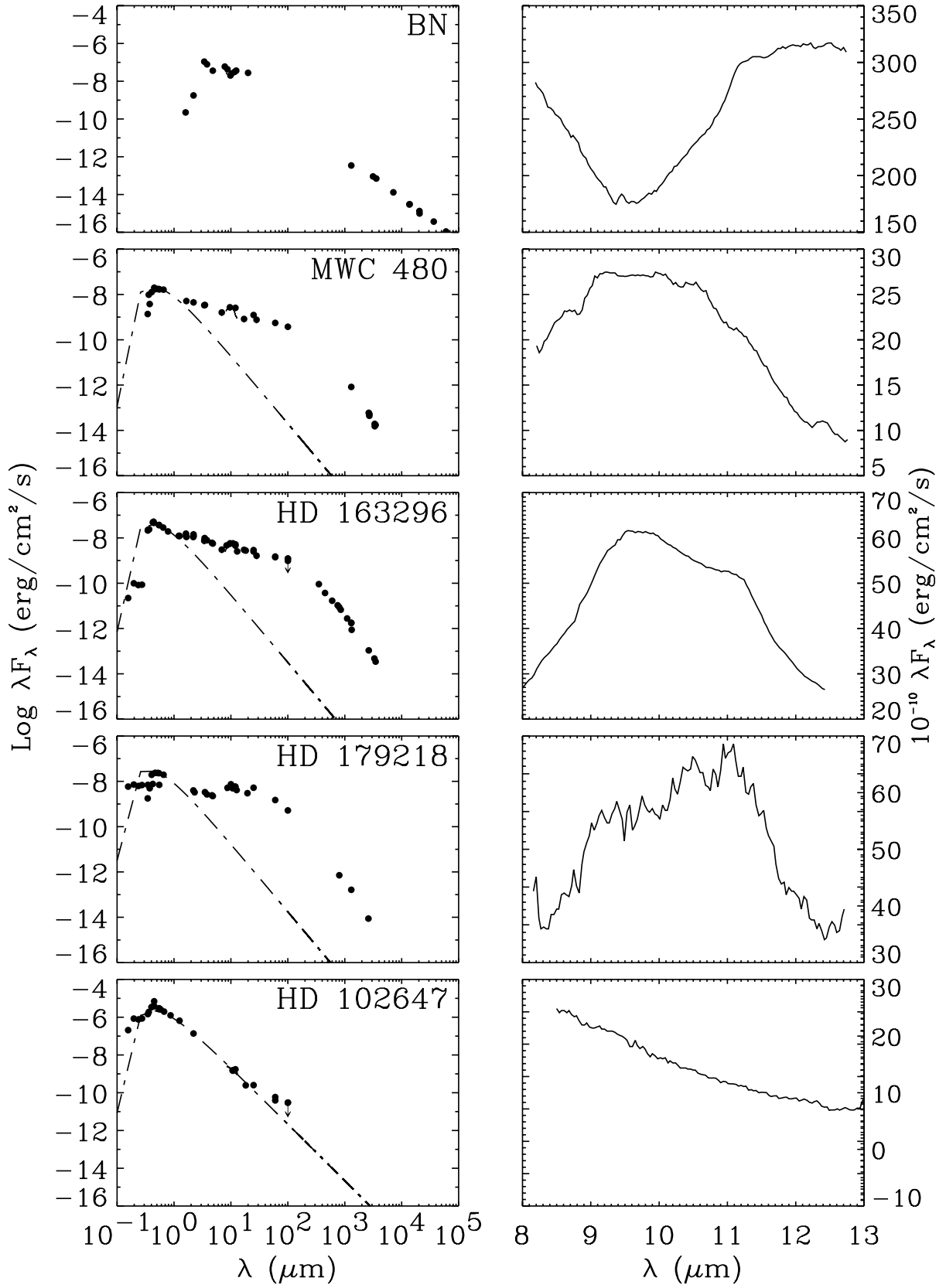
FIG. 8.—Same as Fig. 7, but for evolution of the silicate spectrum for intermediate-mass stars. The evolutionary sequence is similar to that observed for intermediate-mass stars in *ISO* studies (Meeus & Waelkens 1999).

our sample (see Figs. 1 and 2). The spectra of IRAS 04287+ 1801 and IRAS 04381+2540 (and possibly Mon R2 IRS 3) possess a shallow absorption feature near 11.2 μm in addition to the 9.7 μm absorption seen toward the other embedded sources. The additional absorption feature has rarely been seen (e.g., Boogert et al. 2004), and its origin may be related to grain mantle ice constituents and not silicates (A. C. A. Boogert 2004, private communication). In five other low-mass embedded objects the silicate feature appears with absorption superposed on emission between 9 and 12 μm. In the most extreme case, IRAS 04264+2433, the spectrum shows almost pure silicate emission. These spectra may be explained by a source geometry in which cold dust located along the line of sight is absorbing against silicate emission from warmer dust located near the protostar. Radiative transfer modeling is required to explore this scenario and constrain whether the cold dust is in fact associated with these sources or associated with remnant unbound material in the dense core.

The absorption spectra exhibit a variety of morphologies and have been ordered in Figure 1 roughly according to the strength of the absorption feature. This may correspond to an evolutionary sequence from strong ISM-like absorption through superposed absorption+emission and is discussed more quantitatively in § 6.1.

5.2. *Silicate Emission Spectra*

The silicate feature is seen in emission toward five T Tauri stars and five HAEBE stars in our sample (see Figs. 3 and 4). A total of 8 out of 10 of these stars possess significant IR luminosities ($L_{IR}/L_* > 0.1$), with the exception of IRAS 14050−4109 and Hen 3-600A ($L_{IR}/L_* \sim 10^{-2}$, similar to debris disks). The shape of the emission feature varies from smooth single peaks near 9.7 μm, consistent with amorphous olivine, to more complex spectra with additional peaks near 10.2 and 11.3 μm, indicative of enstatite and forsterite components. This suggests that silicate processing is occurring within disks around optically revealed T Tauri and HAEBE stars.

Silicate features similar to those of amorphous olivine were observed toward four of five T Tauri stars (GM Aur, AA Tau, IRAS 14050−4109, and LkCa 15). The emission features are wider in comparison to absorption features in the ISM. This could be due to either the addition of ~10.2–11.3 μm emission from crystalline silicates or broadening of the amorphous emission feature due to increased grain sizes. The absence of a strong crystalline component in the emission spectra indicates that the wider feature is more likely related to grain growth (discussed below) than to crystallization. Crystalline silicates appear to be absent even in the two sources with evidence of disk clearing, IRAS 14050−4109 (with $L_{IR}/L_* \sim 10^{-2}$) and GM Aur (possessing a gap at small radii; Rice et al. 2003).

Possible evidence for crystallization appears in the spectra observed toward four of five HAEBE stars (MWC 480, HD 163296, HD 184761, and WW Vul). HD 163296, HD 184761, and WW Vul each possess an emission feature characteristic of amorphous olivine, as well as a small peak at 11.3 μm, consistent with crystalline forsterite (although this peak is much weaker than that seen for β Pictoris or HD 100546; Knacke et al. 1993; Meeus et al. 2001). MWC 480 possesses a peak near 10.4 μm, which is consistent with crystalline enstatite. The three disks with 11.3 μm peaks are young intermediate-mass stars (~2 $M_\odot$) with SEDs depicting substantial IR emission from warm dust, indicating that the component producing the feature must be present at a young evolutionary stage. Analysis of the crystalline silicate content in these disks, however, may be complicated by the 11.2 μm PAH emission band. Clear identification of the 11.3 μm feature as arising from crystalline silicates can only be obtained if there is evidence of their longer wavelength features, or if the presence of PAHs can be ruled out. HD 163296 and WW Vul have been observed with *ISO*, and no evidence of PAH emission in the 6–12 μm region was detected (Meeus et al. 2001; Acke & van den Ancker 2004); longer wavelength crystalline silicate features were detected toward HD 163296. In the same study, PAH emission at 6.2 μm was detected toward MWC 480, but similar features at 7.6 and 8.5 were not. No previous observations of HD 184761 are available.

Finally, one low-mass T Tauri star (Hen 3-600A) and one HAEBE star (HD 179218), 10 and 6 Myr of age, respectively, each show a strong peak at 11.3 μm that dominates the spectrum. The shape of the emission feature is consistent with that of crystalline forsterite (including the correlating small peak at 10.2 μm). These spectra are similar to that of the first widely recognized crystalline silicate source, HD 100546 (Bouwman et al. 2003). In contrast to the detection of crystalline silicates toward several HAEBE stars, to date crystalline silicates have been detected toward only a small number of approximately solar-mass stars (TW Hya, Sitko et al. 2000; VW Cha and Glass I, Meeus et al. 2003). Our sample seems consistent with this trend, with one of five low-mass star disks and four of five HAEBE star disks showing signs of crystalline silicates. Our sample is small, however, and may not be representative. Observations of a larger sample of low-mass stars are needed to quantify and understand the differences in the composition of dust around low- versus intermediate-mass stars.

5.3. *Featureless Spectra*

The spectra and SEDs for debris disks around low- and intermediate-mass stars are shown in Figures 5 and 6, respectively. No silicate emission was seen toward these disks: their spectra are predominantly photospheric, with a few exhibiting dust continua. The lack of silicate emission may indicate either a paucity of small grains ($a < 10$ μm) or a dearth of optically thin material inside of ~10 AU ($T \geq 200$ K). The absence of a substantial continuum at 10 μm is consistent with the SEDs for HD 102647, HD 17925, HD 22049, and HD 216803, which show very low IR and millimeter excesses ($L_{IR}/L_* < 10^{-3}$) with $\lambda_{onset} \geq 60$ μm. This suggests that the debris disks have lost most of their (warm, small) circumstellar silicate grains. Three debris disks, 49 Ceti, HR 4796A, and HD 233517,[9] however, still possess substantial far-IR and millimeter excesses. This substantial amount of cold dust, combined with the absence of silicate emission, suggests the possible existence of large gaps in these disks at radii close to the star, similar to those modeled in the debris disks around ϵ Eri, Vega, and HR 4796A (Ozernoy et al. 2000; Wyatt et al. 1999; Wyatt 2003).

5.4. *Evolution of Silicate Spectra*

The SEDs and silicate spectra of the sample indicate a possible evolutionary trend; silicate absorption is observed toward embedded protostars, strong silicate emission arises from objects with optically thick protoplanetary disks, and nearly photospheric spectra are observed toward optically thin debris disks. The details of this trend are discussed below for both low- and intermediate-mass stars using a representative subset of our sample as shown in Figures 7 and 8.

---

[9] There is some evidence that HD 233517 may be an Li-rich giant and not a young star with a debris disk. See Balachandran et al. (2000) for details.

Figure 7 shows the evolutionary sequence for material around low-mass stars. The SED for IRAS 04239+2438 indicates an embedded protostar, and the 8–13 μm spectrum depicts deep silicate absorption (similar to seven other embedded sources in our sample). The SED of LkCa 15 is fitted by an optically revealed star and near- to far-IR excess from an optically thick protoplanetary disk (e.g., Chiang et al. 2001), and strong silicate emission is observed toward this source. Similar SEDs and spectra are seen for three other sources. The mid-IR spectrum of IRAS 04295+2251 shows contributions from both silicate emission, peaking near 10.5 μm, and silicate absorption near 9.5 μm and the SED suggests that this source (and five others) may be intermediary between IRAS 04239+2438 and LkCa 15, although the exact geometry is not yet well understood. As discussed above, the SED of Hen 3-600A shows no near-IR excess and very little far-IR flux and silicate emission peaking characteristic of forsterite (peaking near 11.3 μm), indicating substantial dust processing in this disk. Finally, HD 17925 is characteristic of four sources in our sample with SEDs consistent with stellar photospheres (out to 60 μm) toward which no silicate feature is observed, indicating an absence of warm, small circumstellar grains and longer wavelength excess.

A similar evolutionary sequence is shown for the intermediate-mass stars (Fig. 8), from silicate absorption toward the fully embedded Becklin Neugebauer object (BN) to silicate emission in the three optically thick disks and a nearly photospheric spectrum toward the optically thin disk encircling HD 102647. No sources with absorption+emission spectra were seen for the intermediate-mass stars. The sample, however, consisted of only three embedded protostars, and there are large differences in morphology for these absorption spectra. Between the spectra of MWC 480, HD 163296, and HD 179218, the silicate emission feature seems to evolve from amorphous olivine peaking near 9.5 μm to crystalline forsterite, peaking at 11.3 μm, suggesting dust processing, but there appears to be no corresponding evolution of the SEDs. Furthermore, MWC 480 shows silicate emission peaking near 10.5 μm, indicative of crystalline enstatite, not forsterite.

6. QUANTIFYING SILICATE SPECTRA

Having presented our spectra and discussed their overall properties qualitatively, we now embark on a quantitative analysis of the spectra. Detailed interpretation of silicate emission/absorption features necessitates an understanding of the optical depth of the circumstellar envelope or the vertical structure of the circumstellar disk. Because our sample encompasses a variety of complex circumstellar environments ranging from deeply self-embedded young stars to optically thin debris disks, such detailed modeling will not be presented here. Instead, we investigate empirical correlations between several properties of the silicate features and attempt to relate the observed trends to circumstellar properties and dust size and composition. In § 6.1 we begin by evaluating the impact of the source morphology on the structure of the observed silicate feature by investigating correlations between the spectral shape and SED properties. Next, we explore the relationship between the FWHM of the 8–13 μm emission/absorption feature and the central wavelength of the peak/dip (§ 6.2), which are connected to optical depth and dust composition. The relationship between the 9.8 and 11.3 μm fluxes and the peak-to-continuum ratio is indicative of grain size and crystallization fraction, as demonstrated by previous studies of HAEBE and T Tauri stars (Przygodda et al. 2003; van Boekel et al. 2003). Thus, relationships between spectral shape and dust composition and grain size are explored in §§ 6.3 and 6.4. By
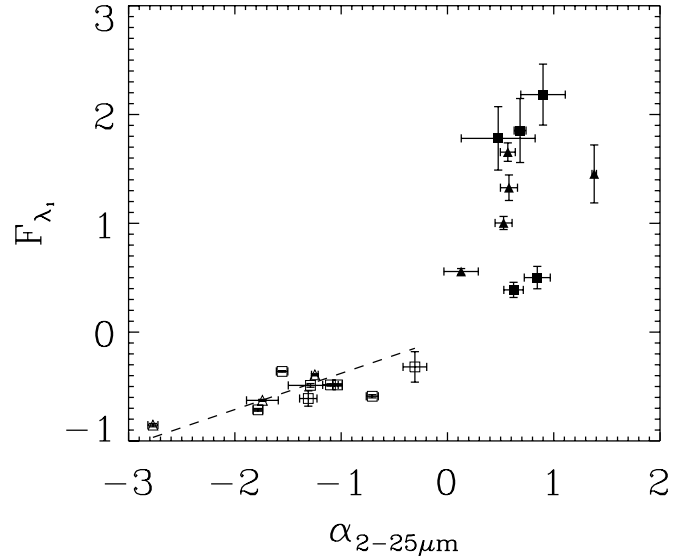

FIG. 9.—Correlations with the SED. This plot shows the correlation between the strength of the silicate feature (F_{λ_1}; defined in Table 5) and the 2–25 μm spectral index ($\alpha_{2-25\,\mu m}$). The open symbols represent absorption spectra of solar-mass (*squares*) and intermediate-mass (*triangles*) stars in our sample. The filled symbols represent emission spectra. Spectra that can be fitted with both emission and absorption are omitted. The error bars for $\alpha_{2-25\,\mu m}$ include the photometric errors as quoted in the literature. Fluxes are calculated by averaging the continuum-normalized spectrum over 0.2 μm. The data are weighted by the inverse square of the errors shown, which include the effects of spectral S/N and the removal of the continuum. For clarity, the error bars for GM Aur have been truncated at $\frac{1}{7}$ of the full error (see text). The strength of the absorption features appears to be strongly correlated with the spectral index ($r = 0.75$, 1.3% probability of being drawn from random distribution), as indicated by the dashed line. In contrast, the strength of the emission features is only weakly correlated with the spectral index, if at all; $r = 0.29$, with a 40% probability that the data are drawn from a random distribution.

applying these methods of analysis to our spectra, we hope to reveal more subtle evolutionary trends than are apparent from simple visual inspection of the data.

6.1. *Silicate Feature Strength and SED Properties*

Based on Figures 7 and 8, we have argued for evidence of an evolutionary sequence in the 10 μm feature from absorption to mixed absorption and emission to pure emission, which may correspond to an evolutionary sequence in SED morphology. To explore this relationship more quantitatively, we investigate possible correlations between 10 μm spectral properties and SED slope or IR excess luminosity.

Lada & Wilking (1984) define a classification system using the SED slope, or 2–25 μm spectral index ($\alpha_{2-25\,\mu m}$). The spectral index is negative for class I sources (embedded stars), positive in the range of 0–1 for class II sources (optically thick disks), and positive and large ($\sim$3) for class III sources (optically thin disks). In Figure 9 we explore possible correlations between the feature strength and the spectral index for spectra with pure emission or absorption features. Spectra showing evidence of mixed absorption and emission are not included. The feature strengths (F_{λ_1}) used here are calculated from the normalized spectra [$F = (F_\nu - F_c)/F_c$], by averaging over a region 0.2 μm wide centered on the largest absolute value ($|F_{\lambda_1}|$) in the normalized spectrum (see Table 5). The spectra were smoothed before fitting to remove large fluctuations due to noise, which may have a large effect on locating the maximum. The quoted errors include the effects of spectral signal-to-noise ratio (S/N) (the standard deviation of the mean), as well as the

TABLE 5
SILICATE SPECTRAL PARAMETERS

Source	λ_1 (μm)	λ_2 (μm)	F_{λ_1}	F_{λ_2}	FWHM	Fit
IRAS 04016+2610.............................	9.34	9.68	−0.49	−0.47	2.43	Absorption
IRAS 04108+2803B[a]........................	9.81	9.77	−0.13	−0.15	0.36	Absorption
	11.67	11.44	0.16	0.15	1.34	Emission
IRAS 04169+2702.............................	9.60	9.58	−0.49	−0.46	2.00	Absorption
IRAS 04181+2654A	9.18	9.52	−0.32	−0.26	2.26	Absorption
IRAS 04181+2654B[a]........................	9.26	9.28	−0.31	−0.30	0.93	Absorption
	11.67	11.44	0.16	0.10	1.34	Emission
IRAS 04239+2436.............................	9.22	9.72	−0.48	−0.45	2.48	Absorption
IRAS 04248+2612[a]...........................	8.74	8.82	−0.19	−0.16	0.85	Absorption
	10.00	10.43	0.22	0.20	1.34	Emission
IRAS 04264+2433.............................	10.26	10.07	0.54	0.51	2.70	Emission
Haro 6-10A	9.41	9.75	−0.59	−0.59	2.36	Absorption
Haro 6-10B	9.37	9.64	−0.36	−0.35	2.20	Absorption
IRAS 04287+1801.............................	9.23	9.93	−0.71	−0.69	3.17	Absorption
IRAS 04295+2251[a]...........................	9.37	9.20	−0.14	−0.14	0.72	Absorption
	10.63	10.78	0.17	0.18	1.26	Emission
AA Tau...	10.15	10.09	0.50	0.49	2.54	Emission
LkCa 15	9.96	10.19	2.18	2.22	2.20	Emission
IRAS 04381+2540.............................	9.71	9.99	−0.61	−0.57	2.93	Absorption
IRAS 04489+3042[a]...........................	9.40	9.20	−0.14	−0.15	0.90	Absorption
	11.69	11.52	0.19	0.23	2.81	Emission
GM Aur...	9.77	9.87	1.78	1.68	2.19	Emission
MWC 480	10.58	10.32	1.00	1.02	2.45	Emission
BN	9.63	9.69	−0.39	−0.41	1.76	Absorption
NGC 2024 IRS 2..............................	9.67	9.87	−0.63	−0.63	2.35	Absorption
Mon R2 IRS 3	9.82	9.93	−0.85	−0.90	2.93	Absorption
Hen 3-600A	10.98	10.62	0.39	0.32	2.07	Emission
IRAS 14050−4109............................	9.62	9.95	1.85	1.86	2.15	Emission
HD 163296	9.61	10.02	1.33	1.34	2.48	Emission
HD 179218	11.01	10.48	0.56	0.53	2.39	Emission
WW Vul...	9.84	9.92	1.65	1.63	2.33	Emission
HD 184761	10.06	10.07	1.45	1.46	2.20	Emission

NOTES.—Parameters λ_1 and F_{λ_1} indicate central wavelengths and feature strengths calculated by fitting a Gaussian to the normalized spectrum. Parameters λ_2 and F_{λ_2} indicate central wavelengths and feature strengths calculated by finding the largest absolute value of the normalized flux. In all cases, FWHMs are found from Gaussian fits.
[a] The observed spectrum can be fitted by absorption+emission.

effects of the continuum normalization method (the errors in determination of the end point fluxes). Error bars are particularly large for GM Aur, for which the spectrum possessed low S/N near the end points used for continuum normalization. For this reason, the error bars for GM Aur shown in all figures have been truncated at $\frac{1}{7}$ of the full error. The correlation is evaluated using a χ^2 linear least-squares regression method. During the calculation of the regressions, each data point is weighted by the inverse square of the error in x and y, so the effects of data with large errors are minimized. One should note that this method may reduce the weighting of T Tauri star disks, as their spectra for the most part have lower S/N than do spectra of disks around HAEBE stars.

There is a strong inverse correlation between the strength of the absorption features and the spectral index. As the spectral index increases, moving from class I toward the realm of class II sources, the strength of absorption features becomes shallower. Furthermore, four of five of the complex spectra (absorption+emission), which are not included in Figure 9, possess spectral indices that are at the low end of the distribution ($\leq$0.5), suggesting that they may be in an intermediate stage between class I and class II. This trend indicates that the strength of silicate absorption is primarily a function of the optical depth and not dust composition/size. In contrast, there is no compelling correlation between strength and spectral index for the emission sources in Figure 9.

Although the strength of the silicate emission features is not related to the spectral index, it may still be dependent on or related to the disk morphology. In order to determine the relationship between the strength of silicate emission and disk morphology, the ratio of the IR to stellar luminosity was calculated. L_{IR}/L_* is related to the optical depth of the disk material for optically thin emission. For optically thick emission, however, L_{IR}/L_* is indicative of the disk geometry, tracing the fraction of light intercepted by the disk (Backman & Paresce 1993). In this case, disk flaring and orientation both affect the IR-to-stellar luminosity ratio, with a maximum value of L_{IR}/L_* of $\frac{1}{2}$ for a flared disk, in which the thickness increases with distance from the star (Kenyon & Hartmann 1987), and $\frac{1}{4}$ for a flat optically thick disk. IR-to-stellar luminosity ratios for the disks in our sample, calculated as described in § 4, are presented in Table 3. The optically thin debris disks possess $L_{IR}/L_* < 0.1$ and do not show evidence of silicate emission. We find generally higher values of L_{IR}/L_* for the optically thick class II disks. These ratios are always greater than 0.1 with a maximum of $\sim$0.5. The strengths of the emission features are not found to be correlated with L_{IR}/L_*. As L_{IR}/L_* is affected by both disk flaring and orientation, we can only say that the combined effect

of the two is not clearly related to the strength of the 10 μm silicate emission feature.

In summary, the strength of silicate absorption can be tied to the self-embeddedness of the star and is probing primarily the optical depth of the absorbing dust. The strength of the emission features appears to trace grain properties (e.g., grain growth and/or crystallinity), as opposed to optical depth, and these properties do not appear to be directly connected to evolutionary stage, as traced by the Lada & Wilking (1984) classification system, or to disk morphology. This is consistent with a scenario in which the observed emission arises from an optically thin region on disk surfaces.

6.2. *Width and Central Wavelength of the Silicate Feature*

For six lines of sight in the ISM, Bowey & Adamson (2002) find that the FWHM of the observed silicate absorption decreases as the features shift to longer wavelength. They also find that these parameters are strongly related to the stellar environment. Three spectra probing the diffuse medium showed silicate absorption features with minima at ~9.8 μm and FWHM of ~2.5 μm, typical of amorphous olivine. The others, within the Taurus molecular cloud, possess silicate absorption features near 9.6 μm with FWHM of 3.3 μm, typical of amorphous pyroxene. The authors suggest that this trend represents an evolution from olivine-dominated silicates in the diffuse ISM to pyroxene-dominated silicates in circumstellar environments.

In order to search for trends in the silicate composition as a function of *circumstellar* environment, we perform similar calculations for the silicate features observed toward our sample of 17 embedded YSOs and 10 optically thick disks. Sources with photospheric spectra are not included. As discussed above, the strength (and shape) of silicate absorption features is a function of the optical depth. The central wavelength of the absorption, however, is dependent on the dust composition. In contrast, the strength and width of silicate emission features (if optically thin) are almost solely dependent on the dust cross section, which is affected by both grain composition and size. The peak of the emission is also believed to be a function of both grain size and composition (van Boekel et al. 2003).

The silicate feature in each normalized spectrum [$F = (F_\nu - F_c)/F_c$] was fitted by a Gaussian to find the FWHM, central wavelength (λ_2), and normalized flux (F_{λ_2}) corresponding to that central wavelength. To account for the structured nature of the silicate features observed, we also record the wavelength (λ_1) corresponding to the largest absolute value ($|F_{\lambda_1}|$; used in § 6.1) in the normalized spectrum. This provides a better characterization in the case of dust with large crystalline-to-amorphous silicate emission ratios (e.g., for HD 179218) where F_{λ_2} lies near the center of the feature at $\lambda_2 \sim 10.5$ μm, but F_{λ_1} successfully traces the stronger flux near the forsterite peak ($\lambda_1 \sim 11$ μm). The results of these calculations are shown in Table 5.

This analysis is not as straightforward for the spectra that show evidence of *both* emission and absorption. If we fit the absorption and emission components individually for the complex spectra, as shown in Table 5, we find small FWHM for the individual features, which are shifted to shorter/longer wavelengths for absorption/emission. For all five of the complex spectra we fit absorption components with $\lambda_{1,2} < 10$ μm and emission components with $\lambda_{1,2} \gtrsim 10$ μm. Although these complex spectra represent an interesting new class of sources, the emission and absorption features clearly cannot be deconvolved empirically. Source geometry must be taken into account in the interpretation of these spectra. For these reasons, we include only pure absorption and emission features in the rest of our analyses.
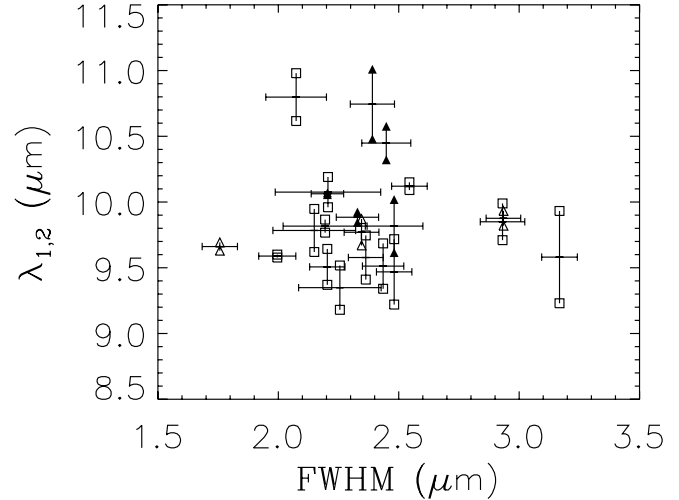

FIG. 10.—Plot of the wavelength of the emission/absorption maxima ($\lambda_{1,2}$) and the width of the feature (FWHM), as presented in Table 5. Parameters λ_1 and λ_2 are represented by connected pairs. Symbols are as described in Fig. 9. Neither the sample of silicate absorption spectra nor that of silicate emission spectra shows significant correlation between $\lambda_{1,2}$ and FWHM. The two samples do show different trends, however, with the emission spectra spanning a larger range in central wavelength and the absorption spectra spanning a larger range in FWHM.

In Figure 10, the central wavelengths (λ_1 and λ_2) of the emission/absorption maxima (as described by F_{λ_1} and F_{λ_2}) are plotted with respect to the FWHM. Although a subset of the pure absorption or emission features are clustered about 9.75 ± 0.15 μm, the sample encompasses a large range of central wavelength (~9–11 μm) and FWHM (~1.7–3 μm), suggesting a range of source environments. There appears to be no strong correlation between $\lambda_{1,2}$ and FWHM in the sample as a whole ($r = 0.04$), nor in either subpopulation of silicate absorption and emission spectra. The two samples do show different trends, however, with the emission spectra spanning a larger range of central wavelength and the absorption spectra spanning a larger range of FWHM. To address the nature of these trends in more detail, we now discuss the absorption and emission subsamples in turn.

The silicate absorption features show little variation in central wavelength (9.6 ± 0.2 μm), which is consistent with amorphous olivines and pyroxenes. The trend seen by Bowey & Adamson (2002) is not seen, suggesting that there is no clear correlation within this sample of class I objects between the grain composition (traced by $\lambda_{1,2}$) and optical depth (traced by FWHM). The FWHM of the absorption features varies significantly (~1.8–3.2 μm), indicating a range of optical depths, indicative of varying envelope thickness or morphology. There are three outlying absorption sources possessing large FWHM (IRAS 04287+1801, IRAS 04381+2540, and Mon R2 IRS 3). These were previously identified in § 5.1 as possessing an additional shallow feature near 11.2 μm, and the very large FWHM may be merely a result of the blending of the 11.2 μm ice feature with the silicate feature.

The silicate emission features in general peak at longer central wavelength (10.2 ± 0.3 μm) in comparison to the embedded sources, indicating either grain growth or modified composition. The silicate emission features also show larger variations in the central wavelength, but little variation in the FWHM. The FWHM for the emission features is largely dependent on the grain cross section and, thus, on both the grain size and composition. The range in FWHM of roughly 2–2.5 μm is consistent with primarily amorphous silicate grains of 0.1–2 μm sizes (van

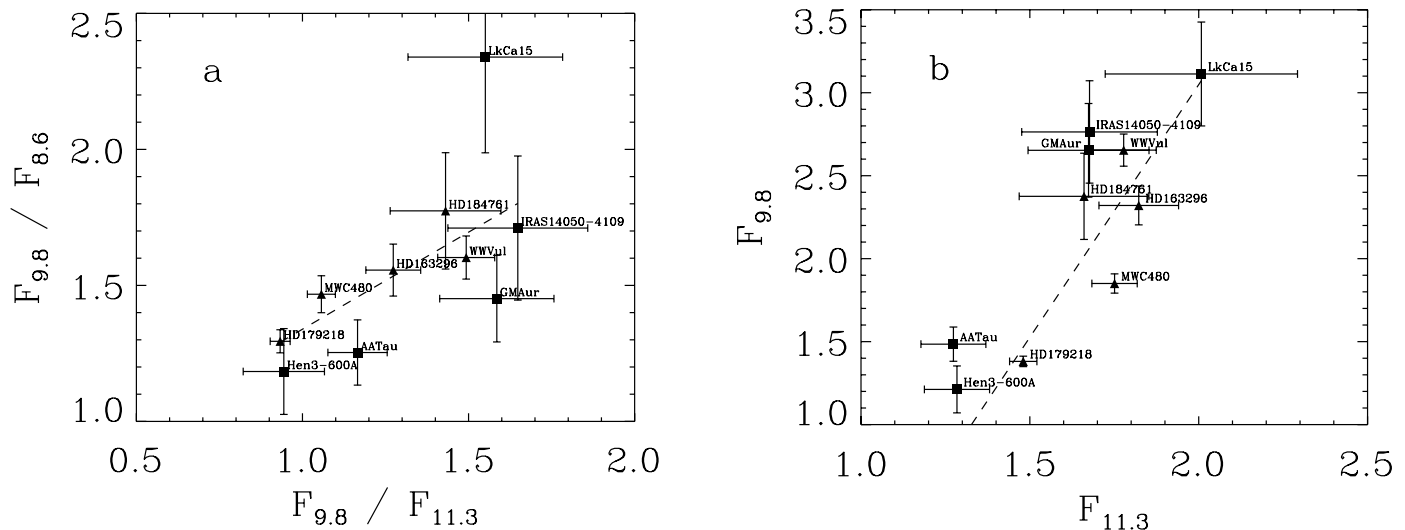Fig. 11.—IR color-color diagrams for silicate emission. (a) Relationship between the slopes on the long- ($F_{9.8}/F_{11.3}$) and short-wavelength ($F_{9.8}/F_{8.6}$) side of the normalized spectra. A linear least-squares fit to the data is depicted by a dashed line, $(F_{9.8}/F_{8.6}) = (0.7 \pm 0.2)(F_{9.8}/F_{11.3}) + (0.6 \pm 0.2)$, and characterized by a correlation coefficient of $r = 0.67$. (b) Fluxes corresponding to amorphous olivine ($F_{9.8}$) and crystalline forsterite ($F_{11.3}$) in the normalized spectra. The linear fit to these data (dashed line; $r = 0.85$), $F_{9.8} = (3.0 \pm 0.6)F_{11.3} - (3.0 \pm 1.0)$, indicates that $F_{11.3}$ does not increase at the expense of $F_{9.8}$. Fluxes and corresponding error bars are calculated as in Fig. 9.

Boekel et al. 2003). The variations in FWHM are also consistent with those expected from the addition of crystalline silicates. Indeed, the two emission spectra with the largest peak wavelengths ($\sim$11.2 μm) are those previously identified as possessing strong crystalline silicate emission, Hen 3-600A and HD 179218. The emission spectrum from MWC 480 is also an outlier, peaking at 10.3–10.5 μm, which is consistent with crystalline enstatite.

Thus, sources with silicate absorption features have central wavelengths and FWHM generally similar to amorphous olivine or pyroxene, while those with silicate emission show increased peak wavelengths and variations in FWHM characteristic of more processed dust. The relationship between the silicate emission feature and size and compositional variations of the dust are explored in more detail below. We do not discuss the absorption or the absorption+emission sources any further.

6.3. Spectral Color-Color Diagrams: Grain Composition

Now we attempt to use fluxes derived from the continuum-normalized silicate emission features as probes of grain composition, following the methods used for *ISO* spectra of HAEBE stars (Bouwman et al. 2001). In particular, we compare fluxes at the nominal wavelengths of emission from amorphous and crystalline olivine, 9.8 and 11.3 μm, and ratios of 9.8 μm/8.6 μm versus 9.8 μm/11.3 μm fluxes in an attempt to assess the crystallization mechanism. Figure 11 displays flux and color-color plots for the silicate emission features observed toward our sample. The fluxes are calculated by averaging over 0.2 μm. The errors are calculated as described in § 6.1 and include the affects of S/N and the continuum subtraction method.

In Figure 11a the relationship between the blue and red slopes is examined. Assuming that the emission arises primarily from amorphous olivine (peaking near 9.8 μm), the slopes on the long- and short-wavelength side of the normalized spectra can be approximated by $F_{9.8}/F_{11.3}$ and $F_{9.8}/F_{8.6}$, respectively. The dashed line indicates the correlation ($r = 0.68$) between the blue and red slopes for the observed silicate emission features. This trend implies that decreasing $F_{9.8}/F_{8.6}$ (blue slopes) correspond to decreasing $F_{9.8}/F_{11.3}$ (red slopes), indicating that the entire feature becomes flatter as emission at 11.3 μm becomes more prominent. The two sources with silicate features that

peak above 11 μm, HD 179218 and Hen 3-600A, also fall along this trend, occupying the lower left corner of the plot. Although the variations in the structure of the silicate emission have often been attributed to variations in the crystalline fraction, this trend is consistent with grain compositions dominated by amorphous olivine, with variations due to changes in grain size (e.g., van Boekel et al. 2003).

If the above trend can be attributed to the conversion from dust dominated by amorphous olivine to that dominated by crystalline forsterite, then variations in the crystallinity of the dust in these sources should be evident in the relationship between the fluxes at these wavelengths. The fluxes corresponding to the peaks of the amorphous olivine ($F_{9.8}$) and crystalline forsterite features ($F_{11.3}$) for the normalized spectra are shown in Figure 11b. There is a linear correlation between the fluxes at 11.3 and 9.8 μm indicating that the flux at 11.3 μm does *not* increase at the expense of the flux at 9.8 μm, as we would expect from crystallization of amorphous olivines (emitting near 9.8 μm). Additionally, the spectra with dominant emission at 11.3 μm are weaker overall and fall in the lower left corner of the plot. This suggests either that the crystalline silicates observed toward these sources are not produced from the same reservoir of small amorphous grains that emits at 9.8 μm, or that variation in the shape of the silicate feature is not dominated by crystallization.

The above analysis demonstrates that the 9.8 μm/8.6 μm and 9.8 μm/11.3 μm colors are correlated within the observed silicate emission features. The features become flatter as the relative emission at 11.3 μm increases, which is consistent with increased grain sizes. Furthermore, the flux at 11.3 μm does not decrease at the expense of that at 9.8 μm, indicating that if the flattening of the feature is due to crystallization, then the crystalline forsterite emitting at 11.3 μm is not crystallized from the amorphous silicate population emitting at 9.8 μm.

6.4. Strength and Shape: Grain Size

Here we discuss the possibility that the changes in the silicate emission feature shape discussed above are due to changes in grain size, rather than crystallinity. Although observations of broadened 8–13 μm silicate features with emission observed
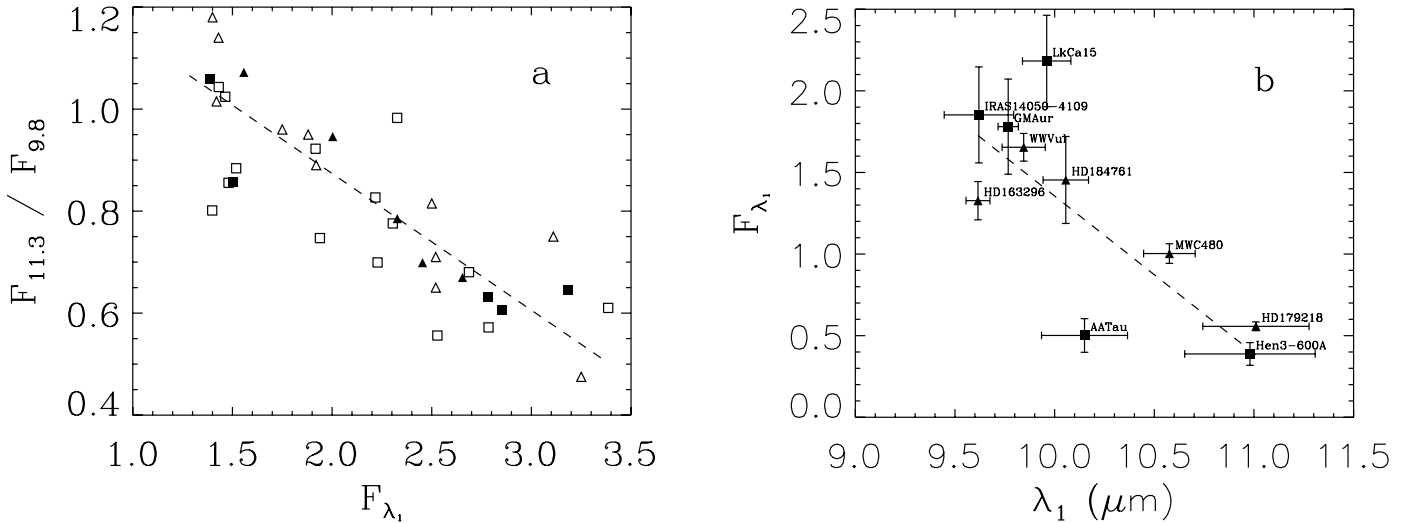
Fig. 12.—Emission feature characteristics. In both panels, the filled squares and triangles represent the observations of T Tauri and HAEBE stars in our sample. (a) Correlation between feature shape ($F_{11.3}/F_{9.8}$) and strength (F_{λ_1}), as noted previously for HAEBE (van Boekel et al. 2003; *open triangles*) and T Tauri stars (Przygodda et al. 2003; *open squares*). The dashed line is a linear fit to the entire sample, $F_{11.3}/F_{9.8} = (1.41 \pm 0.07)F_{\lambda_1} - (0.27 \pm 0.03)$, with a correlation coefficient of $r = 0.82$. (b) Strength of the silicate feature decreases with decreasing peak wavelength (λ_1) as $F_{\lambda_1} = (-1.0 \pm 0.1)\lambda_1 + (11 \pm 1)$, with $r = 0.78$. Both trends are consistent with grain growth (see text). Fluxes and corresponding error bars are calculated as in Fig. 9.

at 11.3 μm were long believed to be a clear indication of the presence of crystalline forsterite, the analysis presented in § 6.3 and recent studies by van Boekel et al. (2003) suggest that such features are actually representative of increased grain size. These studies show that the mid-IR absorption coefficient of ∼0.1 μm–sized amorphous olivine grains possesses a triangular shape similar to that observed in the diffuse ISM. Because of a general decrease in the absorption cross section, a population of larger amorphous olivine grains (∼2.0 μm) has an absorption coefficient that is weaker by a factor of ∼2.3 and flattened between 9.5 and 12 μm. Examination of the emission spectra of 12 HAEBE stars showed that there is a correlation between the feature strength (peak flux of the normalized spectrum) and shape (as indicated by the ratio of the flux at 11.2 to 8.9 μm), with broader emission features being weaker as shown in Figure 12a (*open triangles*). Przygodda et al. (2003) found a similar trend for a sample of disks surrounding low-mass stars (*open squares*).

We perform a similar analysis for our sample of T Tauri and HAEBE stars, which are shown by filled squares and triangles in Figure 12a. Fluxes and errors are calculated as described in § 6.3. The entire sample of both T Tauri and HAEBE star spectra can be fitted by a single trend. This trend is consistent with variations in grain size among the sample, but we cannot rule out the possibility that the changes in feature shape and strength result from an increased crystallization fraction (§ 6.3). The two sources with spectra consistent with forsterite emission at 11.3 μm do not deviate significantly from this trend. It is therefore reasonable to think of the strong, narrow and the broad, weak silicate emission features as arising from "unprocessed" and "processed" dust, respectively. The contributions from dust size and composition can thus only be separated when emission from crystalline silicates is clearly seen in the spectrum as an isolated feature at 11.3 μm.

Although generally used as a measure of the crystallization fraction in the emitting silicate dust (e.g., the "9.8 to 11.3 μm phase transition"), the wavelength of maximum emission may also be affected by grain size. In Figure 12b the maximum emission in the normalized spectrum F_{λ_1} is plotted with respect to the wavelength corresponding to the maximum λ_1. Figure 12b

indicates that for our sample as the feature maximum shifts to longer wavelengths, the strength of the emission feature decreases. This trend is consistent with the effects of grain growth. As the grain size increases, the feature flattens and the maximum decreases in flux and shifts to longer wavelength. Although the two sources with strong crystalline forsterite features (HD 179218 and Hen 3-600A) have weaker peak flux and show up at the bottom right in Figure 12b, in general moving along the trend from the upper left to lower right of Figure 12b does not coincide with the appearance of emission from crystalline forsterite. HD 163296, which has a visible bump near 11.3 μm, has a silicate feature that is still quite strong (in the upper left of the plot). Furthermore, the broad silicate emission feature observed toward AA Tau, which shows no evidence of emission from crystalline forsterite, is quite weak and lies in the middle of the trend. Therefore, the shift in the wavelength of maximum emission in the 10 μm region, or the 9.8 to 11.3 μm phase transition, appears to be largely dependent on grain size variations and thus is in fact *not* a good indicator of the crystallization fraction.

If the trends depicted in Figure 12 primarily indicate a change in the grain size, then they suggest a progressive removal of small grains (<2 μm) from the warm ($T \approx 300$ K) disk surface probed by the 10 μm feature. Dust settling would preferentially remove larger grains from the disk surface. The absence of small grains could be related to the removal of dust through gap clearing, but if so we would expect GM Aur, which shows evidence of a substantial gap, to display a broadened feature indicative of larger grains. The flat, broadened spectra in the bottom right of Figure 12b are therefore most likely a result of grain growth in the surfaces of these disks.

7. CONCLUSIONS AND FURTHER WORK

Spectra in the range of 8–13 μm were obtained for 34 low- and intermediate-mass YSOs. The evolutionary sequence seen in *ISO* observations of high/intermediate-mass YSOs (Meeus & Waelkens 1999) was confirmed and extended here to approximately solar-mass stars. Amorphous silicate absorption is observed toward young, embedded sources. In 5 of 17 embedded sources, complex spectra that may be interpreted as a combination of silicate absorption and emission are observed.

These spectra may represent an interesting new class of sources that are in between class I and class II, but they require physical models to deconvolve the emission and absorption. Silicates are observed in emission toward optically revealed stars. The shape of these emission features varies from strong triangular emission peaked near 9.8 μm to flat, broad emission with a central wavelength between 10 and 11 μm. Finally, silicate emission was absent for the debris disks in our sample.

To aid in the interpretation of the silicate features, we explore the connections between silicate feature properties with stellar evolution through comparison with the SEDs. We find that the strength of 10 μm silicate absorption is strongly correlated with the 2–25 μm spectral index. Class I sources with complex absorption+emission features have small spectral indices when compared to those with pure absorption, suggesting that the former are less embedded. These results indicate that the silicate absorption feature is indeed a good probe of the circumstellar environment, tracing the self-embeddedness of the star. In contrast, the strength of the silicate emission feature does not appear to be correlated with the 2–25 μm spectral index (evolutionary stage) or the IR-to-stellar luminosity ratio (disk geometry) and thus probes grain properties rather than source morphology.

Although the strength of the silicate absorption features is dependent on the circumstellar environment, the central wavelength of the emission should be sensitive to the grain composition. We therefore attempted to quantify the effects of grain properties, such as size and composition, on the shape and/or central wavelength of all of the silicate features observed in our sample. In general, the features are clustered around 9.7 μm, corresponding to amorphous olivine, with FWHM near ∼2.3 μm. A direct correlation between FWHM and central wavelength is seen for neither silicate emission nor absorption features. The pure silicate absorption features exhibit a large range of FWHM, likely related to differences in optical depth, and a narrow range of central wavelengths, indicating limited variation in grain size and/or composition from that of the ISM. A larger scatter and higher mean central wavelength are found for the emission spectra, likely related to compositional variations within the sample (i.e., fraction of amorphous vs. crystalline silicates), indicating increased dust processing.

As the emission features are more sensitive to grain properties, we further analyzed the structure of the emission features, finding the following:

1. The shape of the silicate emission of most T Tauri stars was similar to that previously observed in the diffuse ISM, in contrast to the structured emission feature observed for most HAEBE stars. This suggests an absence of small (<10 μm), warm ($T \approx 300$ K) *crystalline* silicates in these T Tauri star disks, but colder or larger crystalline silicate grains may still be present and, if so, will be visible through far-infrared lattice modes accessible from space-borne observations.

2. A correlation between the peak shape as traced by $F_{11.3}/F_{9.8}$ and feature strength for five T Tauri and five HAEBE stars in our sample was also found. This is consistent with that seen for several HAEBE stars (van Boekel et al. 2003) and T Tauri stars (Przygodda et al. 2003), which are attributed to changes in grain

size (from 0.1–2 μm). The entire sample can be fitted best with a single trend, including spectra with strong indications of crystalline forsterite. The wavelength of maximum emission was also found to be correlated with peak strength for our sample. This indicates that interpretation of the 9.8 to 11.3 μm phase transition must therefore include analysis of grain size in addition to crystallization fraction.

3. We also demonstrate that the flux at 11.3 μm does not increase at the expense of that at 9.8 μm. If crystallization is dominating the transition, then this indicates that the crystalline forsterite emitting near 11.3 μm was likely not formed from the population of amorphous olivine emitting near 9.8 μm, suggesting a more complex crystallization mechanism. Another interpretation is that the relationship between the 11.3 and 9.8 μm fluxes is *dominated* by grain size effects and not crystallization.

Silicate emission features in solar-mass T Tauri stars have primarily been observed in the 10 μm atmospheric window (as in this study). Because of sensitivity limitations, *ISO* studies of silicates focused on intermediate- or high-mass stars. The *Spitzer Space Telescope* will be used to expand these studies for a large sample of low-mass stars, ranging from embedded protostars to optically thin disks, via the combination of various GTO programs and the C2D ($\tau_{\rm dust} > 1$) and FEPS ($\tau_{\rm dust} < 1$) Legacy programs.[10] In this manner, the study of the crystalline and amorphous silicates in disks will be expanded to include disks around low-mass, Sun-like stars, creating a database analogous to *ISO* studies of high/intermediate-mass stars. These studies will include longer wavelength silicate bands, which depend intricately on the coordination of the silicon atoms and can provide more specific information about the minerals present, including the Mg/Fe ratio. The mineral content of the grains in each stage of evolution can thus be directly compared to that of meteorites, asteroids, and comets.

---

[10] Details of the C2D and FEPS programs can be found at http://peggysue .as.utexas.edu/SIRTF and http://feps.as.arizona.edu, respectively.

APPENDIX A

VARIABILITY OF 8–13 μm SILICATE EMISSION SPECTRA

Long-term monitoring of several sources, including DG Tau (Wooden et al. 2000) and HD 45677 (Sitko et al. 1994), has revealed dramatic variations in the strength and shape of silicate features over periods of months to years. Observations of DG Tau revealed that
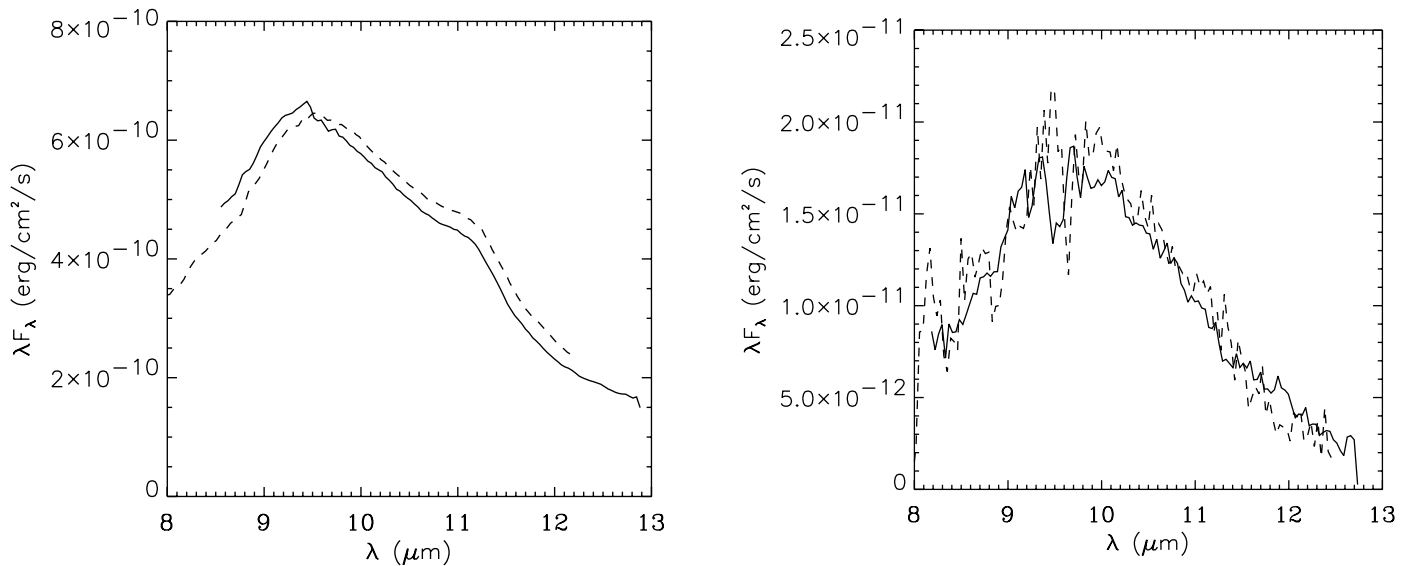
FIG. 13.—Searches for variability. The left panel shows the silicate emission toward HD 163296 observed on 1999 August 23 (*solid line*) and 2000 June 20 (*dashed line*). The right panel shows the silicate emission observed toward LkCa 15 on 1999 November 30 (*solid line*) and 2000 November 8 (*dashed line*). The spectra from two observing runs are overlaid, showing that there is no significant variability (above the error) in the shape of the silicate emission feature for these two sources on a yearly timescale. The continuum was not subtracted for these spectra.

although the dust continuum remained fairly constant, the silicate feature evolved from nearly featureless continuum, to emission from crystalline and amorphous silicates, to emission from primarily amorphous silicates, and finally to absorption from amorphous silicates between 1996 and 2000. Wooden et al. (2000) indicate that these variations in the silicate feature are due to dust in the optically thin disk surface and that the continuum is produced by the underlying disk midplane (e.g., Calvet et al. 1992). For HD 45677, the flux of the silicate emission feature was observed to decrease by ∼30% between 1980 and 1992, coincident with an increase in the stellar flux of ∼60% (Sitko et al. 1994). The authors suggest a scenario in which long-term (decade long) variations in UV and optical flux are due to a clear hole moving into the line of sight, which is possibly coupled with a loss of small grains, as indicated by the change in flux of the silicate feature.

Multiple spectra were obtained toward a few sources in our sample, permitting study of the variability in shape and strength of the silicate emission. Figure 13 shows the silicate emission toward HD 163296 and LkCa 15 for two observations taken approximately 1 yr apart. Spectra from the two observing runs are overlaid, showing that they are consistent (within the errors). The double-peaked structure seen in the spectrum of HD 163296 has been previously observed in spectra obtained by *ISO* (Bouwman et al. 2001; 1996 October 14) and ground-based observations (Sitko et al. 1999; 1996 October 10), and these spectra do not differ significantly from our observations.

HD 179218, Hen 3-600A, and MWC 480 have also been observed on more than one occasion reported in the literature. The previous observations of HD 179218 (Bouwman et al. 2001; *ISO* LWS, 1996 October 5) are virtually identical to our observations (2000 February 21). The spectra depict very similar peak strengths and shapes. MWC 480, however, exhibits very different emission in the Sitko et al. (1999; Infrared Telescope Facility [IRTF] BAAS, 1996 October 14) study than in our spectrum (1999 November 30). In particular, the 11.3 μm feature (crystalline forsterite) is much less prominent in our observations and there is an additional peak at ∼10.5 μm (near the position of crystalline enstatite). However, the (peak to continuum) strength of the feature is the same to within ∼15%. The observations of Hen 3-600A by Honda et al. (2003; Subaru COMICS, 2001 December 27) also suggest strong evidence of variability when compared to our data (Fig. 3; 2000 February 21). Our spectrum shows much less emission at 9.2 and possibly 10.3 μm (both attributed to enstatite), with the peak at 11.3 μm (forsterite) dominating the spectrum. There also appears to be an accompanying decrease in the continuum or in the strength of emission near 12.5 μm from 2000 to 2001.

There is no obvious trend in the variability with respect to spectral parameters or silicate emission feature shape from these observations. HD 179218 and Hen 3-600A have similar emission features and ages and are in similar evolutionary stages (although their mass differs by a factor of 2). However, the spectrum of Hen 3-600A is highly variable on 1 yr timescales while the spectrum of HD 179218 has not changed in more than 3 yr. Although HD 163296 and MWC 480 possessed similar spectra in 1996 (Sitko et al. 1999), the spectra for these sources are quite different from each other in 1999 (our data). MWC 480 has undergone changes in the spectrum that indicate conversion between the crystalline forms of forsterite (Mg_2SiO_4) and enstatite ($MgSiO_3$). This conversion, also seen in the Hen 3-600A spectrum, is the opposite of the expected transition with time during the standard annealing process (see Gail 1998).

Studies of the variability of silicate emission may provide valuable information about the mechanisms of grain growth and/or crystallization that affect the feature shape. However, variability of the silicate emission feature has been observed toward only a few objects and rarely in a comprehensive program designed to monitor the accompanying variability of the star and/or SED. Dedicated long-term monitoring of the silicate feature toward a larger sample of objects is required to understand the cause of silicate feature variability in disks.

APPENDIX B

SED REFERENCES

The SEDs presented in Figures 1–6 were compiled from photometric observations in the literature. The references for each source are listed below.

49 Ceti.—The SED includes optical photometry from Hayes & Latham (1975), *UBV* photometry from Rybka (1969) and Stoy (1969), *JHKLM* photometry from Eiroa et al. (2001) and Sylvester et al. (1996), mid-IR photometry from Thi et al. (2001), and *IRAS* observations from Beichman et al. (1988).

HD 17925.—The SED includes optical photometry from Hayes & Latham (1975), *UBVRIJHKL* photometry from Johnson et al. (1966, 1968), Cutispoto et al. (2001), and Bessel (1990), *N*-band photometry from Metchev et al. (2004), and *IRAS* observations from Beichman et al. (1988) as presented in Habing et al. (2001).

HD 22049.—The SED includes optical photometry from Hayes & Latham (1975), Geneva seven-color photometry (*U*, *B*1, *B*, *B*2, *V*1, *V*, *G*) from Rufener (1976), *UBVRIJHKL* photometry from Johnson et al. (1966), Mendoza (1970), and Glass (1975), *IRAS* photometry from Beichman et al. (1988) and Habing et al. (2001), and 800–1300 μm photometry from Chini et al. (1990).

IRAS 04016+2610.—The SED includes optical, *JHKL*, (sub)millimeter photometry from Kenyon et al. (1993 and references therein), 1–2 μm photometry from Padgett et al. (1999), mid-IR photometry from Myers et al. (1987) and this paper, submillimeter photometry from Young et al. (2003) and Hogerheijde & Sandell (2000), and millimeter photometry from Moriarty-Schieven et al. (1994), Motte & André (2001), Hogerheijde et al. (1997), Ohashi et al. (1996), Saito et al. (2001), and Lucas et al. (2000).

IRAS 04108+2803.—The SED includes optical, *JHKL*, (sub)millimeter photometry from Kenyon et al. (1993 and references therein), mid-IR photometry from Myers et al. (1987) and this paper, *IRAS* photometry from Beichman et al. (1988), submillimeter photometry from Young et al. (2003), and millimeter photometry from Moriarty-Schieven et al. (1994), Motte & André (2001), and Ohashi et al. (1996).

IRAS 04169+2702.—The SED includes *K*-band photometry from Tamura et al. (1991), *K*-band, millimeter, and submillimeter photometry from Barsony & Kenyon (1992), *IRAS* photometry from Beichman et al. (1988), submillimeter photometry from Young et al. (2003), millimeter photometry from Moriarty-Schieven et al. (1994) and Motte & André (2001), and radio photometry from Saito et al. (2001).

IRAS 04181+2654A/B.—The SEDs include *JHK*-band photometry from Kenyon et al. (1993 and references therein), *IRAS* photometry from Beichman et al. (1988), and submillimeter photometry from Moriarty-Schieven et al. (1994).

IRAS 04239+2436.—The SED includes *JHKL*-band photometry from Kenyon et al. (1993) and Padgett et al. (1999), *IRAS* photometry from Beichman et al. (1988), submillimeter photometry from Young et al. (2003) and Moriarty-Schieven et al. (1994), millimeter photometry from Motte & André (2001), Ohashi et al. (1996), and Saito et al. (2001), and radio photometry from Lucas et al. (2000).

IRAS 04248+2612.—The SED includes *JHKL*-band photometry from Kenyon et al. (1993) and Padgett et al. (1999), *N*-band photometry from this paper, *IRAS* photometry from Beichman et al. (1988), submillimeter photometry from Young et al. (2003), Moriarty-Schieven et al. (1994), and Dent et al. (1998), millimeter photometry from Motte & André (2001) and Ohashi et al. (1996), and radio photometry from Lucas et al. (2000).

IRAS 04264+2433.—The SED includes *JHKL*-band photometry from Kenyon et al. (1993 and references therein), *N*-band photometry from this paper, *IRAS* photometry from Beichman et al. (1988), submillimeter photometry from Young et al. (2003), and millimeter photometry from Motte & André (2001).

Haro 6-10A/B.—The SEDs include *BVRIJH* and mid-IR photometry from Myers et al. (1987), *KLM* photometry Kenyon et al. (1993) and Leinert & Haas (1989), *IRAS* photometry from Beichman et al. (1988), and (sub)millimeter photometry from Chandler et al. (1998) and Kenyon et al. (1993).

IRAS 04287+1801.—The SED includes *JHKLM*-band photometry from Kenyon et al. (1993), *N*-band photometry from this paper, *IRAS* photometry from Beichman et al. (1988), and (sub)millimeter photometry from Chandler & Richer (2000), Moriarty-Schieven et al. (1994), Motte & André (2001), Hogerheijde et al. (1997), Ohashi et al. (1996), and Saito et al. (2001).

IRAS 04295+2251.—The SED includes *JHKL* and mid-IR photometry from Kenyon et al. (1993 and references therein), *N*-band photometry from this paper, *IRAS* photometry from Beichman et al. (1988), submillimeter photometry from Young et al. (2003) and Moriarty-Schieven et al. (1994), and millimeter photometry from Motte & André (2001) and Ohashi et al. (1996).

AA Tau.—The SED includes *UBV* photometry from Joy (1949), mid-IR photometry from Thi et al. (2001) and Metchev et al. (2004), *IRAS* photometry from Beichman et al. (1988), and (sub)millimeter photometry from Dutrey et al. (1996), Beckwith & Sargent (1991), Beckwith et al. (1990), and Qi (2001).

LkCa 15.—The SED includes *UBVRIJHKLN* photometry from Kenyon & Hartmann (1995 and references therein), mid-IR photometry from Thi et al. (2001), *IRAS* photometry from Beichman et al. (1988), and millimeter photometry from Osterloh & Beckwith (1995), Duvert et al. (2000), and Qi (2001).

IRAS 04381+2450.—The SED includes *JHKL* and mid-IR photometry from Kenyon et al. (1993 and references therein), *IRAS* photometry from Beichman et al. (1988), and (sub)millimeter photometry from Young et al. (2003), Moriarty-Schieven et al. (1994), Hogerheijde & Sandell (2000), and Hogerheijde et al. (1997).

IRAS 04489+3042.—The SED includes *JHKL* and mid-IR photometry from Kenyon et al. (1993 and references therein), *N*-band photometry from this paper, and millimeter photometry from Motte & André (2001).

GM Aur.—The SED includes *UBV* photometry from Bastian & Mundt (1979), *UBVRIJHK* photometry from Kenyon & Hartmann (1995), mid-IR photometry from Thi et al. (2001), *IRAS* photometry from Beichman et al. (1988), and (sub)millimeter photometry from Beckwith & Sargent (1991), Dutrey et al. (1996), Beckwith et al. (1990), and Qi (2001).

MWC 480.—The SED includes optical photometry from Eimontas & Sudzius (1998) and Haupt & Schroll (1974), *HKL* photometry from Allen (1973), mid-IR photometry from Thi et al. (2001), *IRAS* photometry from Beichman et al. (1988), and millimeter photometry from Mannings & Sargent (1997) and Qi (2001).

BN.—The SED includes near-IR photometry from Hillenbrand et al. (2001) and Dougados et al. (1993), mid-IR photometry from Gezari et al. (1998), millimeter photometry from Plambeck et al. (1995), and radio photometry from Felli et al. (1993) and Menten & Reid (1995).

NGC 2024 IRS 2.—The SED includes optical photometry from L. A. Hillenbrand (2004, unpublished; CCD), *JHKL* photometry from Haisch et al. (2001), mid- and far-IR photometry from Grasdalen (1974), Haisch et al. (2001), and Thronson et al. (1978, 1984), millimeter photometry from Wilson et al. (1995) and Eisner & Carpenter (2003), and radio photometry from Gaume et al. (1992), Rodríguez et al. (2003), and Snell & Bally (1986).

Mon R2 IRS 3.—The SED includes *JHKLM* photometry from Preibisch et al. (2002), Carpenter et al. (1997), and Koresko et al. (1993), mid-IR photometry from Walsh et al. (2001) and Persi et al. (1996), *IRAS* photometry from Beichman et al. (1988), (sub)millimeter photometry from Jenness et al. (1995) and Henning et al. (1992), and radio photometry from Tofani et al. (1995).

HD 233517.—The SED includes optical photometry from Sylvester et al. (1996) and Miroshnichenko et al. (1996), *JHKLL'MN* photometry from Skinner et al. (1995) and Sylvester et al. (1996), *IRAS* photometry from Beichman et al. (1988), and millimeter photometry from Duncan et al. (1990) and Sylvester et al. (2001).

Hen 3-600A.—The SED includes *BVRI* photometry from Gregorio-Hetem et al. (1992) and Torres et al. (2003), *JHKLMN* photometry from Geoffray & Monin (2001), Webb et al. (1999), Weintraub et al. (2000), Jayawardhana et al. (1999), and Metchev et al. (2004), and *IRAS* photometry from Beichman et al. (1988).

HD 102647.—The SED includes optical photometry from Hayes & Latham (1975), Geneva seven-color photometry (U, B1, B, B2, V1, V, G) from Rufener (1976), *UBVRIJK* photometry from Johnson et al. (1966), mid-IR photometry from Jayawardhana et al. (2001) and Metchev et al. (2004), *IRAS* photometry from Beichman et al. (1988), and 60 μm *ISO* photometry from Habing et al. (2001).

HR 4796A.—The SED includes optical photometry from Hayes & Latham (1975), *UBVRIJHK* photometry from Jura et al. (1993), *KLMN* and mid-IR photometry from Fajardo-Acosta et al. (1998), *N*-band photometry from Metchev et al. (2004), *IRAS* photometry from Beichman et al. (1988), and submillimeter photometry from Jura et al. (1995).

IRAS 14050−4109.—The SED includes optical photometry from Gregorio-Hetem & Hetem (2002), *N*-band photometry from Metchev et al. (2004), and *IRAS* photometry from Beichman et al. (1988).

HD 163296.—The SED includes optical photometry from Jamar et al. (1995), Haupt & Schroll (1974), The et al. (1985), Malfait et al. (1998), and Oudmaijer et al. (2001), *UBVRI* photometry from Hillenbrand et al. (1992), *JHKLMN* photometry from Berrilli et al. (1992), Eiroa et al. (2001), and Allen (1973), mid-IR photometry from Thi et al. (2001) and Jayawardhana et al. (2001), *IRAS* photometry from Beichman et al. (1988), and (sub)millimeter photometry from Mannings & Emerson (1994) and Qi (2001).

HD 179218.—The SED includes optical photometry from Hayes & Latham (1975), *UPXYZVS* photometry from Eimontas & Sudzius (1998), *UBVRIJHKLMN* photometry from Miroshnichenko et al. (1999), Malfait et al. (1998), and Lawrence et al. (1990), *IRAS* photometry from Beichman et al. (1988), submillimeter photometry from Meeus et al. (2001), and millimeter photometry from Mannings & Sargent (2000).

WW Vul.—The SED includes *UPXYZVS* photometry from Eimontas & Sudzius (1998), *UBVR* photometry from Herbst & Shevchenko (1999), *JHKL* photometry from Eiroa et al. (2001) and Glass & Penston (1974), mid-IR photometry from Thi et al. (2001), *IRAS* photometry from Beichman et al. (1988), and millimeter photometry from Natta et al. (1997, 2001).

HD 184761.—The SED includes optical photometry from Hayes & Latham (1975), *UBVRIJHK* photometry from Miroshnichenko et al. (1999), and *IRAS* photometry from Beichman et al. (1988).

HD 216803.—The SED includes *UPXYZVS* photometry from Eimontas & Sudzius (1998), *UBVRI* photometry from Johnson et al. (1966) and Bessel (1990), mid-IR photometry from Fajardo-Acosta et al. (1999) and Metchev et al. (2004), *IRAS* photometry from Beichman et al. (1988), 60 μm *ISO* photometry from Habing et al. (2001), and millimeter photometry from Weintraub et al. (1994).

REFERENCES

Acke, B., & van den Ancker, M. E. 2004, A&A, 426, 151
Allen, D. A. 1973, MNRAS, 161, 145
Augereau, J. C., Nelson, R. P., Lagrange, A. M., Papaloizou, J. C. B., & Mouillet, D. 2001, A&A, 370, 447
Backman, D. E., & Paresce, F. 1993, in Protostars and Planets III, ed. E. H. Levy & J. I. Lunine (Tucson: Univ. Arizona Press), 1253
Balachandran, S. C., Fekel, F. C., Henry, G. W., & Uitenbroek, H. 2000, ApJ, 542, 978
Barrado y Navascues, D., Stauffer, J. R., Hartmann, L., & Balachandran, S. C. 1997, ApJ, 475, 313
Barsony, M., & Kenyon, S. J. 1992, ApJ, 384, L53
Bastian, U., & Mundt, R. 1979, A&AS, 36, 57
Beckwith, S. V. W., Henning, T., & Nakagawa, Y. 2000, in Protostars and Planets IV, ed. V. Mannings, A. P. Boss, & S. S. Russell (Tucson: Univ. Arizona Press), 533
Beckwith, S. V. W., & Sargent, A. I. 1991, ApJ, 381, 250
Beckwith, S. V. W., Sargent, A. I., Chini, R. S., & Guesten, R. 1990, AJ, 99, 924
Beichman, C. A., Neugebauer, G., Habing, H. J., Clegg, P. E., & Chester, T. J. 1988, NASA Ref. Publ., 1190, 1
Berrilli, F., Corciulo, G., Ingrosso, G., Lorenzetti, D., Nisini, B., & Strafella, F. 1992, ApJ, 398, 254

Bessel, M. S. 1990, A&AS, 83, 357
Boogert, A. C. A., et al. 2004, ApJS, 154, 359
Bouwman, J., de Koter, A., Dominik, C., & Waters, L. B. F. M. 2003, A&A, 401, 577
Bouwman, J., Meeus, G., de Koter, A., Hony, S., Dominik, C., & Waters, L. B. F. M. 2001, A&A, 375, 950
Bowey, J. E., & Adamson, A. J. 2002, MNRAS, 334, 94
Bowey, J. E., Adamson, A. J., & Whittet, D. C. B. 1998, MNRAS, 298, 131
Calvet, N., Magris, G. C., Patino, A., & D'Alessio, P. 1992, Rev. Mex. AA, 24, 27
Carpenter, J. M., Meyer, M. R., Dougados, C., Strom, S. E., & Hillenbrand, L. A. 1997, AJ, 114, 198
Chandler, C. J., Barsony, M., & Moore, T. J. T. 1998, MNRAS, 299, 789
Chandler, C. J., & Richer, J. S. 2000, ApJ, 530, 851
Chiang, E. I., Joung, M. K., Creech-Eakman, M. J., Qi, C., Kessler, J. E., Blake, G. A., & van Dishoeck, E. F. 2001, ApJ, 547, 1077
Chini, R., Kruegel, E., & Kreysa, E. 1990, A&A, 227, L5
Cohen, M. 1980, MNRAS, 191, 499
Cohen, M., & Witteborn, F. C. 1985, ApJ, 294, 345
Coulson, I. M., Walther, D. M., & Dent, W. R. F. 1998, MNRAS, 296, 934
Cutispoto, G., Messina, S., & Rodonò, M. 2001, A&A, 367, 910
D'Alessio, P., Calvet, N., & Hartmann, L. 2001, ApJ, 553, 321

Dent, W. R. F., Matthews, H. E., & Ward-Thompson, D. 1998, MNRAS, 301, 1049

Dougados, C., Lena, P., Ridgway, S. T., Christou, J. C., & Probst, R. G. 1993, ApJ, 406, 112

Duncan, W. D., Sandell, G., Robson, E. I., Ade, P. A. R., & Griffin, M. J. 1990, MNRAS, 243, 126

Dutrey, A., Guilloteau, S., Duvert, G., Prato, L., Simon, M., Schuster, K., & Menard, F. 1996, A&A, 309, 493

Duvert, G., Guilloteau, S., Ménard, F., Simon, M., & Dutrey, A. 2000, A&A, 355, 165

Eimontas, A., & Sudzius, J. 1998, Baltic Astron., 7, 407

Eiroa, C., et al. 2001, A&A, 365, 110

Eisner, J. A., & Carpenter, J. M. 2003, ApJ, 598, 1341

Fabian, D., Henning, T., Jäger, C., Mutschke, H., Dorschner, J., & Wehrhan, O. 2001, A&A, 378, 228

Fajardo-Acosta, S. B., Stencel, R. E., Backman, D. E., & Thakur, N. 1999, ApJ, 520, 215

Fajardo-Acosta, S. B., Telesco, C. M., & Knacke, R. F. 1998, AJ, 115, 2101

Felli, M., Taylor, G. B., Catarzi, M., Churchwell, E., & Kurtz, S. 1993, A&AS, 101, 127

Gail, H.-P. 1998, A&A, 332, 1099

Gaume, R. A., Johnston, K. J., & Wilson, T. L. 1992, ApJ, 388, 489

Geoffray, H., & Monin, J. L. 2001, A&A, 369, 239

Gezari, D. Y., Backman, D. E., & Werner, M. W. 1998, ApJ, 509, 283

Glass, I. S. 1975, MNRAS, 171, 19P

Glass, I. S., & Penston, M. V. 1974, MNRAS, 167, 237

Grasdalen, G. L. 1974, ApJ, 193, 373

Gregorio-Hetem, J., & Hetem, A. 2002, MNRAS, 336, 197

Gregorio-Hetem, J., Lepine, J. R. D., Quast, G. R., Torres, C. A. O., & de La Reza, R. 1992, AJ, 103, 549

Habing, H. J., et al. 2001, A&A, 365, 545

Haisch, K. E., Lada, E. A., Piña, R. K., Telesco, C. M., & Lada, C. J. 2001, AJ, 121, 1512

Hanner, M. S., Brooke, T. Y., & Tokunaga, A. T. 1995, ApJ, 438, 250

———. 1998, ApJ, 502, 871

Hartmann, L. 2002, ApJ, 578, 914

Hartmann, L., Calvet, N., Gullbring, E., & D'Alessio, P. 1998, ApJ, 495, 385

Haupt, H. F., & Schroll, A. 1974, A&AS, 15, 311

Hayes, D. S., & Latham, D. W. 1975, ApJ, 197, 593

Henning, T., Chini, R., & Pfau, W. 1992, A&A, 263, 285

Herbst, W., & Shevchenko, V. S. 1999, AJ, 118, 1043

Hillenbrand, L. A., Carpenter, J. M., & Skrutskie, M. F. 2001, ApJ, 547, L53

Hillenbrand, L. A., Strom, S. E., Vrba, F. J., & Keene, J. 1992, ApJ, 397, 613

Hogerheijde, M. R., & Sandell, G. 2000, ApJ, 534, 880

Hogerheijde, M. R., van Dishoeck, E. F., Blake, G. A., & van Langevelde, H. J. 1997, ApJ, 489, 293

Honda, M., Kataza, H., Okamoto, Y. K., Miyata, T., Yamashita, T., Sako, S., Takubo, S., & Onaka, T. 2003, ApJ, 585, L59

Jaeger, C., Mutschke, H., Begemann, B., Dorschner, J., & Henning, T. 1994, A&A, 292, 641

Jamar, C., Macau-Hercot, D., Monfils, A., Thompson, G. I., Houziaux, L., & Wilson, R. 1995, VizieR Online Data Catalog, 3039, 0

Jayawardhana, R., Fisher, R. S., Telesco, C. M., Piña, R. K., Barrado y Navascués, D., Hartmann, L. W., & Fazio, G. G. 2001, AJ, 122, 2047

Jayawardhana, R., Hartmann, L., Fazio, G., Fisher, R. S., Telesco, C. M., & Piña, R. K. 1999, ApJ, 521, L129

Jenness, T., Scott, P. F., & Padman, R. 1995, MNRAS, 276, 1024

Johnson, H. L., Iriarte, B., Mitchell, R. I., & Wisniewskj, W. Z. 1966, Comm. Lunar Planet. Lab., 4, 99

Johnson, H. L., MacArthur, J. W., & Mitchell, R. I. 1968, ApJ, 152, 465

Joy, A. H. 1949, ApJ, 110, 424

Jura, M., Ghez, A. M., White, R. J., McCarthy, D. W., Smith, R. C., & Martin, P. G. 1995, ApJ, 445, 451

Jura, M., Zuckerman, B., Becklin, E. E., & Smith, R. C. 1993, ApJ, 418, L37

Kalas, P., & Jewitt, D. 1995, AJ, 110, 794

Kemper, F., Vriend, W. J., & Tielens, A. G. G. M. 2004, ApJ, 609, 826

Kenyon, S. J., Calvet, N., & Hartmann, L. 1993, ApJ, 414, 676

Kenyon, S. J., & Hartmann, L. 1987, ApJ, 323, 714

———. 1995, ApJS, 101, 117

Knacke, R. F., Fajardo-Acosta, S. B., Telesco, C. M., Hackwell, J. A., Lynch, D. K., & Russell, R. W. 1993, ApJ, 418, 440

Koresko, C. D., Beckwith, S., Ghez, A. M., Matthews, K., Herbst, T. M., & Smith, D. A. 1993, AJ, 105, 1481

Lada, C. J., & Wilking, B. A. 1984, ApJ, 287, 610

Lawrence, G., Jones, T. J., & Gehrz, R. D. 1990, AJ, 99, 1232

Leinert, C., & Haas, M. 1989, ApJ, 342, L39

Lucas, P. W., Blundell, K. M., & Roche, P. F. 2000, MNRAS, 318, 526

Malfait, K., Waelkens, C., Waters, L. B. F. M., Vandenbussche, B., Huygen, E., & de Graauw, M. S. 1998, A&A, 332, L25

Mannings, V., & Emerson, J. P. 1994, MNRAS, 267, 361

Mannings, V., & Sargent, A. I. 1997, ApJ, 490, 792

———. 2000, ApJ, 529, 391

Marcy, G. W., Cochran, W. D., & Mayor, M. 2000, in Protostars and Planets IV, ed. V. Mannings, A. P. Boss, & S. S. Russell (Tucson: Univ. Arizona Press), 1285

Meeus, G., Sterzik, M., Bouwman, J., & Natta, A. 2003, A&A, 409, L25

Meeus, G., & Waelkens, C. 1999, in The Universe as Seen by ISO, ed. P. Cox & M. F. Kessler (ESA SP-427; Noordwijk: ESA), 373

Meeus, G., Waters, L. B. F. M., Bouwman, J., van den Ancker, M. E., Waelkens, C., & Malfait, K. 2001, A&A, 365, 476

Mendoza, E. E. 1970, Bol. Obs. Tonantzintla Tacubaya, 5, 269

Menten, K. M., & Reid, M. J. 1995, ApJ, 445, L157

Metchev, S. A., Hillenbrand, L. A., & Meyer, M. R. 2004, ApJ, 600, 435

Miroshnichenko, A. S., Bergner, Y. K., & Kuratov, K. S. 1996, A&A, 312, 521

Miroshnichenko, A. S., Mulliss, C. L., Bjorkman, K. S., Morrison, N. D., Kuratov, K. S., & Wisniewski, J. P. 1999, MNRAS, 302, 612

Molster, F. J., et al. 1999, Nature, 401, 563

Moriarty-Schieven, G. H., Wannier, P. G., Keene, J., & Tamura, M. 1994, ApJ, 436, 800

Motte, F., & André, P. 2001, A&A, 365, 440

Mouillet, D., Larwood, J. D., Papaloizou, J. C. B., & Lagrange, A. M. 1997, MNRAS, 292, 896

Myers, P. C., Fuller, G. A., Mathieu, R. D., Beichman, C. A., Benson, P. J., Schild, R. E., & Emerson, J. P. 1987, ApJ, 319, 340

Natta, A., Grinin, V. P., Mannings, V., & Ungerechts, H. 1997, ApJ, 491, 885

Natta, A., Meyer, M. R., & Beckwith, S. V. W. 2000, ApJ, 534, 838

Natta, A., Prusti, T., Neri, R., Wooden, D., Grinin, V. P., & Mannings, V. 2001, A&A, 371, 186

Ohashi, N., Hayashi, M., Kawabe, R., & Ishiguro, M. 1996, ApJ, 466, 317

Osterloh, M., & Beckwith, S. V. W. 1995, ApJ, 439, 288

Oudmaijer, R. D., et al. 2001, A&A, 379, 564

Ozernoy, L. M., Gorkavyi, N. N., Mather, J. C., & Taidakova, T. A. 2000, ApJ, 537, L147

Padgett, D. L., Brandner, W., Stapelfeldt, K. R., Strom, S. E., Terebey, S., & Koerner, D. 1999, AJ, 117, 1490

Pegourie, B., & Papoular, R. 1985, A&A, 142, 451

Persi, P., Busso, M., Corcione, L., Ferrari-Toniolo, M., & Marenzi, A. R. 1996, A&A, 306, 587

Plambeck, R. L., Wright, M. C. H., Mundy, L. G., & Looney, L. W. 1995, ApJ, 455, L189

Pollack, J. B., Hollenbach, D., Beckwith, S., Simonelli, D. P., Roush, T., & Fong, W. 1994, ApJ, 421, 615

Preibisch, T., Balega, Y. Y., Schertl, D., & Weigelt, G. 2002, A&A, 392, 945

Przygodda, F., van Boekel, R., Àbrahàm, P., Melnikov, S. Y., Waters, L. B. F. M., & Leinert, C. 2003, A&A, 412, L43

Qi, C. 2001, Ph.D. thesis, Caltech

Reach, W. T., Morris, P., Boulanger, F., & Okumura, K. 2003, Icarus, 164, 384

Rice, W. K. M., Wood, K., Armitage, P. J., Whitney, B. A., & Bjorkman, J. E. 2003, MNRAS, 342, 79

Rodríguez, L. F., Gómez, Y., & Reipurth, B. 2003, ApJ, 598, 1100

Rufener, F. 1976, A&AS, 26, 275

Rybka, E. 1969, Acta Astron., 19, 229

Saito, M., Kawabe, R., Kitamura, Y., & Sunada, K. 2001, ApJ, 547, 840

Santos, N. C., Israelian, G., & Mayor, M. 2004, A&A, 415, 1153

Simon, M., Dutrey, A., & Guilloteau, S. 2000, ApJ, 545, 1034

Sitko, M. L., Grady, C. A., Lynch, D. K., Russell, R. W., & Hanner, M. S. 1999, ApJ, 510, 408

Sitko, M. L., Halbedel, E. M., Lawrence, G. F., Smith, J. A., & Yanow, K. 1994, ApJ, 432, 753

Sitko, M. L., Lynch, D. K., & Russell, R. W. 2000, AJ, 120, 2609

Skinner, C. J., Sylvester, R. J., Graham, J. R., Barlow, M. J., Meixner, M., Keto, E., Arens, J. F., & Jernigan, J. G. 1995, ApJ, 444, 861

Snell, R. L., & Bally, J. 1986, ApJ, 303, 683

Stauffer, J. R., Hartmann, L. W., & Barrado y Navascues, D. 1995, ApJ, 454, 910

Stoy, R. H. 1969, Mon. Notes Astron. Soc. South Africa, 27, 119

Strom, K. M., Strom, S. E., Edwards, S., Cabrit, S., & Skrutskie, M. F. 1989, AJ, 97, 1451

Sylvester, R. J., Dunkin, S. K., & Barlow, M. J. 2001, MNRAS, 327, 133

Sylvester, R. J., & Mannings, V. 2000, MNRAS, 313, 73

Sylvester, R. J., Skinner, C. J., Barlow, M. J., & Mannings, V. 1996, MNRAS, 279, 915

Tamura, M., Gatley, I., Waller, W., & Werner, M. W. 1991, ApJ, 374, L25

The, P. S., Cuypers, H., Tjin A Djie, H. R. E., & Felenbok, P. 1985, A&A, 149, 429

Thi, W. F., et al. 2001, ApJ, 561, 1074

Thronson, H. A., Campbell, M. F., & Harvey, P. M. 1978, AJ, 83, 1581
Thronson, H. A., Schwartz, P. R., Smith, H. A., Glaccum, W., Harper, D. A., Loewenstein, R. F., Smith, J., & Lada, C. J. 1984, ApJ, 280, 154
Tofani, G., Felli, M., Taylor, G. B., & Hunter, T. R. 1995, A&AS, 112, 299
Torres, G., Guenther, E. W., Marschall, L. A., Neuhäuser, R., Latham, D. W., & Stefanik, R. P. 2003, AJ, 125, 825
Uchida, K. I., et al. 2004, ApJS, 154, 439
van Boekel, R., Waters, L. B. F. M., Dominik, C., Bouwman, J., de Koter, A., Dullemond, C. P., & Paresce, F. 2003, A&A, 400, L21
van den Ancker, M. E., Bouwman, J., Wesselius, P. R., Waters, L. B. F. M., Dougherty, S. M., & van Dishoeck, E. F. 2000, A&A, 357, 325
van den Ancker, M. E., de Winter, D., & Tjin A Djie, H. R. E. 1998, A&A, 330, 145
Walsh, A. J., Bertoldi, F., Burton, M. G., & Nikola, T. 2001, MNRAS, 326, 36
Webb, R. A., Zuckerman, B., Platais, I., Patience, J., White, R. J., Schwartz, M. J., & McCarthy, C. 1999, ApJ, 512, L63
Weidenschilling, S. J., & Cuzzi, J. N. 1993, in Protostars and Planets III, ed. E. H. Levy & J. I. Lunine (Tucson: Univ. Arizona Press), 1031
Weinberger, A. J., Becklin, E. E., & Zuckerman, B. 2003, ApJ, 584, L33
Weintraub, D. A., Saumon, D., Kastner, J. H., & Forveille, T. 2000, ApJ, 530, 867

Weintraub, D. A., Tegler, S. C., Kastner, J. H., & Rettig, T. 1994, ApJ, 423, 674
Whittet, D. C. B., Bode, M. F., Longmore, A. J., Admason, A. J., McFadzean, A. D., Aitken, D. K., & Roche, P. F. 1988, MNRAS, 233, 321
Whittet, D. C. B., et al. 1997, ApJ, 490, 729
Willner, S. P., et al. 1982, ApJ, 253, 174
Wilson, T. L., Mehringer, D. M., & Dickel, H. R. 1995, A&A, 303, 840
Wolf, S., & Hillenbrand, L. A. 2003, ApJ, 596, 603
Wooden, D. H. 1994, in ASP Conf. Ser. 62, The Nature and Evolutionary Status of Herbig Ae/Be Stars, ed. P. S. The, M. R. Perez, & E. P. J. Van den Heuvel (San Francisco: ASP), 138
———. 2002, Earth Moon Planets, 89, 247
Wooden, D. H., Bell, K. R., Harker, D. E., & Woodward, C. E. 2000, BAAS, 32, 1482
Wyatt, M. C. 2003, ApJ, 598, 1321
Wyatt, M. C., Dermott, S. F., Telesco, C. M., Fisher, R. S., Grogan, K., Holmes, E. K., & Piña, R. K. 1999, ApJ, 527, 918
Young, C. H., Shirley, Y. L., Evans, N. J., & Rawlings, J. M. C. 2003, ApJS, 145, 111
Zuckerman, B., Song, I., Bessell, M. S., & Webb, R. A. 2001, ApJ, 562, L87